Astronomy & Astrophysics

Three short-period Jupiters from TESS

HIP 65Ab, TOI-157b, and TOI-169b

L. D. Nielsen[1], R. Brahm[2,3], F. Bouchy[1], N. Espinoza[4], O. Turner[1], S. Rappaport[5], L. Pearce[6], G. Ricker[5],
R. Vanderspek[5], D. W. Latham[7], S. Seager[6,8,9], J. N. Winn[10], J. M. Jenkins[11], J. S. Acton[12], G. Bakos[10], T. Barclay[13,14],
K. Barkaoui[15,16], W. Bhatti[10], C. Briceño[17], E. M. Bryant[18,19], M. R. Burleigh[12], D. R. Ciardi[20],
K. A. Collins[9], K. I. Collins[21], B. F. Cooke[18,19], Z. Csubry[10], L. A. dos Santos[1], Ph. Eigmüller[22], M. M. Fausnaugh[5],
T. Gan[23], M. Gillon[15], M. R. Goad[12], N. Guerrero[5], J. Hagelberg[1], R. Hart[24], T. Henning[25], C. X. Huang[5], E. Jehin[26],
J. S. Jenkins[27,28], A. Jordán[2,3], J. F. Kielkopf[29], D. Kossakowski[25], B. Lavie[1], N. Law[30], M. Lendl[1,31], J. P. de Leon[32],
C. Lovis[1], A. W. Mann[30], M. Marmier[1], J. McCormac[18,19], M. Mori[32], M. Moyano[33], N. Narita[34,35,36,37,38], D. Osip[39],
J. F. Otegi[1,40], F. Pepe[1], F. J. Pozuelos[25,15], L. Raynard[12], H. M. Relles[7], P. Sarkis[25], D. Ségransan[1], J. V. Seidel[1],
A. Shporer[5], M. Stalport[1], C. Stockdale[41], V. Suc[2], M. Tamura[32,34,36], T. G. Tan[42], R. H. Tilbrook[12], E. B. Ting[11],
T. Trifonov[25], S. Udry[1], A. Vanderburg[43], P. J. Wheatley[18,19], G. Wingham[44], Z. Zhan[8,9], and C. Ziegler[45]

(Affiliations can be found after the references)

ABSTRACT

We report the confirmation and mass determination of three hot Jupiters discovered by the Transiting Exoplanet Survey Satellite (TESS) mission: HIP 65Ab (TOI-129, TIC-201248411) is an ultra-short-period Jupiter orbiting a bright ($V = 11.1$ mag) K4-dwarf every 0.98 days. It is a massive $3.213 \pm 0.078\ M_J$ planet in a grazing transit configuration with an impact parameter of $b = 1.17^{+0.10}_{-0.08}$. As a result the radius is poorly constrained, $2.03^{+0.61}_{-0.49}\ R_J$. The planet's distance to its host star is less than twice the separation at which it would be destroyed by Roche lobe overflow. It is expected to spiral into HIP 65A on a timescale ranging from 80 Myr to a few gigayears, assuming a reduced tidal dissipation quality factor of $Q'_s = 10^7-10^9$. We performed a full phase-curve analysis of the TESS data and detected both illumination- and ellipsoidal variations as well as Doppler boosting. HIP 65A is part of a binary stellar system, with HIP 65B separated by 269 AU (3.95 arcsec on sky). TOI-157b (TIC 140691463) is a typical hot Jupiter with a mass of $1.18 \pm 0.13\ M_J$ and a radius of $1.29 \pm 0.02\ R_J$. It has a period of 2.08 days, which corresponds to a separation of just 0.03 AU. This makes TOI-157 an interesting system, as the host star is an evolved G9 sub-giant star ($V = 12.7$). TOI-169b (TIC 183120439) is a bloated Jupiter orbiting a $V = 12.4$ G-type star. It has a mass of $0.79 \pm 0.06\ M_J$ and a radius of $1.09^{+0.08}_{-0.05}\ R_J$. Despite having the longest orbital period ($P = 2.26$ days) of the three planets, TOI-169b receives the most irradiation and is situated on the edge of the Neptune desert. All three host stars are metal rich with [Fe/H] ranging from 0.18 to 0.24.

Key words. planets and satellites: detection – planets and satellites: individual: TOI-129 – planets and satellites: individual: HIP 65A – planets and satellites: individual: TOI-157

1. Introduction

Since July 2018, the Transiting Exoplanet Survey Satellite (TESS; Ricker et al. 2015) has surveyed the Southern and Northern Hemispheres for exoplanets transiting bright stars. Based on the first year of observations in the south (Sectors 1–13), a total number of 1117 TESS objects-of-interest (TOIs; Guerrero et al. 2020) have been identified. Currently, 667 of these are still considered as planet candidates and 55 have been confirmed as new TESS-planets and four as transiting brown dwarfs (including studies in preparation and published results, see e.g. Cañas et al. 2019; Jones et al. 2019; Esposito et al. 2019; Günther et al. 2019; Eisner et al. 2020; Díaz et al. 2020; Nielsen et al. 2020; Šubjak et al. 2020; Carmichael et al. 2020). We note that 146 of the TOIs from Sectors 1–13 are previously known planets.

A recent study by Zhou et al. (2019) offers a first estimate of the occurrence rate of hot Jupiters discovered by TESS by analysing a sample of bright ($T_{mag} < 10$) main sequence stars

observed by TESS. They find an occurrence rate of $0.40 \pm 0.10\%$ which is in agreement with statistics based on the *Kepler* mission (Fressin et al. 2013; Santerne et al. 2016). An even rarer sub-population of hot Jupiters are the ultra-short-period (USP) Jupiters with orbital periods shorter than one day. To date, the following eight such planets are known: WASP-18b (Hellier et al. 2009), WASP-19b (Hebb et al. 2010), WASP-43b (Hellier et al. 2011), WASP-103b (Gillon et al. 2014), HATS-18b (Penev et al. 2016), KELT-16b (Oberst et al. 2017), NGTS-6b (Vines et al. 2019), and NGTS-10b (McCormac et al. 2020).

Hot Jupiters, and in particular USP Jupiters, can offer insights into planet-star interactions such as photo-evaporation and atmospheric escape (Bourrier et al. 2020; Owen & Lai 2018; Murray-Clay et al. 2009), atmospheric structure and chemistry (Parmentier et al. 2018; Kataria et al. 2015; Kreidberg et al. 2014; Murgas et al. 2014), and tidal decay (Yee et al. 2020). These planets shape the upper edge of the Neptune desert (Mazeh et al. 2016; Szabó & Kiss 2011) which constitutes a dearth of sub-Jovian planets at short periods. The proposed mechanisms

Table 1. Stellar properties for HIP 65A, TOI-157, and TOI-169.

Property	HIP 65A	TOI-157	TOI-169	Source
Spectral type	K4V	G9IV	G1V	Pecaut & Mamajek (2013)
2MASS ID	J00004490-5449498	J04544830-7640498	J01070679-7511559	2MASS
Gaia ID DR2	4923860051276772608	4624979393181971328	4684513614202233728	*Gaia*
TIC ID	201248411	140691463	183120439	TESS
TOI	TOI-129	TOI-157	TOI-169	TESS
Astrometric properties				
RA	00:00:44.56	04:54:48.34	01:07:06.88	TESS
Dec	−54:49:50.93	−76:40:50.17	−75:11:56.19	TESS
μ_{RA} (mas yr^{-1})	−202.82 ± 0.03	11.71 ± 0.035	20.23 ± 0.05	*Gaia*
μ_{Dec} (mas yr^{-1})	−71.52 ± 0.03	−18.92 ± 0.05	−15.61 ± 0.05	*Gaia*
Parallax (mas)	16.156 ± 0.021	2.783 ± 0.022	2.424 ± 0.025	*Gaia*
Photometric properties				
B (mag)	12.29 ± 0.15	13.45 ± 0.03[†]	13.06 ± 0.02	*Tycho*/APASS [†]
V (mag)	11.13 ± 0.06	12.73 ± 0.05[†]	12.36 ± 0.05	*Tycho*/APASS [†]
G (mag)	10.590 ± 0.004	12.514 ± 0.003	12.238 ± 0.018	*Gaia*
T (mag)	9.901 ± 0.006	12.017 ± 0.006	11.788 ± 0.006	TESS
J (mag)	8.92 ± 0.02	11.37 ± 0.02	11.18 ± 0.01	2MASS
H (mag)	8.40 ± 0.03	10.99 ± 0.03	10.90 ± 0.02	2MASS
K_s (mag)	8.29 ± 0.03	10.89 ± 0.02	10.82 ± 0.02	2MASS
W1 (mag)	8.12 ± 0.02	10.85 ± 0.03	10.80 ± 0.03	WISE
W2 (mag)	8.18 ± 0.02	10.89 ± 0.03	10.84 ± 0.03	WISE
W3 (mag)	8.10 ± 0.02	10.87 ± 0.07	10.75 ± 0.08	WISE
W4 (mag)	8.12 ± 0.21			WISE

Notes. Results for stellar parameters modelled in this study can be found in Table 3. Spectral type is based on T_{eff} from global modelling (see Sect. 4) and Table 5 in Pecaut & Mamajek (2013). [†]B- and V-magnitudes are from the *Tycho* catalouge for HIP 65A and TOI-169. For TOI-157 the APASS measurement is used.
References. *Tycho* (Høg et al. 2000); 2MASS (Skrutskie et al. 2006); WISE (Wright et al. 2010); *Gaia* (Gaia Collaboration 2018); APASS (Henden & Munari 2014).

creating the desert are numerous, but they can generally be regarded as a combination of the following three dominant processes: photo-evaporation which strips less massive planets of their outer layers (Lundkvist et al. 2016; Owen & Lai 2018); the availability of disc material during planet formation (Armitage 2007); and planet migration (Demangeon et al. 2018; Alexander, & Armitage 2009).

Massive close-in planets also challenge current planet formation models; they represent the bulk of the mass and angular momentum in their systems while shaping their formation and evolution over time. An extreme case is NGTS 1b, which is a hot Jupiter around a M0 star (Bayliss et al. 2018). Both in-situ formation and scenarios where the Jupiter is formed far out in the system followed by subsequent inward migration are still being considered in order to explain the presence of hot Jupiters (Bailey & Batygin 2018; Nagasawa et al. 2008).

In this work, we present one USP and two hot Jupiters orbiting bright stars observed by TESS in its first year of operation. Table 1 lists the host stars stellar parameters. We modelled the systems self consistently with *EXOFASTv2* using transit light curves and radial velocity (RV) measurements to obtain masses and radii for all three systems. Our analysis is based on RV data from the high resolution spectrographs CORALIE on the Swiss 1.2 m telescope and FEROS on the 2.2 m MPG/ESO telescope, both in La Silla, Chile. In addition to the TESS data, we also utilise data from ground based photometric facilities that are part of the TESS Follow-up Observing Program, including LCOGT, NGTS, CHAT, Trappist-South, IRSF, PEST, Mt. Stuart Observatory, MKO, and Hazelwood Observatory. Additionally, SOAR speckle imaging was used to rule out close stellar companions.

2. Observations

A summary of all the data used in the joint analysis of HIP 65Ab, TOI-157b, and TOI-169b can be found in Table 2. Additionally SOAR speckle imaging was used to rule out close stellar companions, as described in Sect. 2.4.

2.1. Discovery photometry from TESS

HIP 65A, TOI-157 and TOI-169 were all observed by TESS in multiple Sectors and announced as TOIs from Sector 1 by the TESS Science Office. HIP 65A (TOI-129, TIC 201248411) was observed with 2-min cadence in Sectors 1 and 2 from 2018-Jul.-25 to 2018-Sep.-20. TOI-157 (TIC 140 691 463) was observed in Sectors 1–8 in the full frame images (FFI) with 30-min cadence and in Sectors 9, 11, 12, and 13 with 2-min cadence. TOI-169 was observed in the FFIs in Sector 1 and later in Sector 13 with 2-min cadence.

For the Sectors with 2-min data available we use the publicly available Simple Aperture Photometry flux with pre-search data conditioning (PDC-SAP; Stumpe et al. 2014, 2012; Smith et al. 2012; Jenkins et al. 2010) provided by the Science Processing Operations Center (SPOC; Jenkins et al. 2016). For the FFI data we utilised light curves produced by the MIT Quick Look pipe-line.

2.2. Follow-up spectroscopy with CORALIE & FEROS

HIP 65A, TOI-157 and TOI-169 were observed with the high resolution spectrograph CORALIE on the Swiss 1.2 m Euler telescope at La Silla Observatory (Queloz et al. 2001a).

Table 2. Summary of the discovery TESS-photometry, follow-up photometry and radial velocity observations of HIP 65A, TOI-157, and TOI-169.

Date	Source	N.Obs / Filter
HIP 65A (TOI-129)		
2018 July – Sep	TESS 2 min	TESS
2018 Nov.–Dec.	CORALIE	17
2018 Nov.–Dec.	FEROS	17
2018 Sep. 7	LCO-SSO	z'
2018 Sep. 10	MKO	r'
2018 Sep. 13	LCO-SSO	B
2018 Sep. 13	LCO-SSO	i'
2018 Sep. 14	LCO-SSO	B
2018 Sep. 14	LCO-SSO	i'
2018 Sep. 14	PEST	V
2018 Nov. 30	NGTS	NGTS
2018 Dec. 2	NGTS	NGTS
TOI-157		
2018 Jul.–2019 Feb.	TESS FFI	TESS
2019 Mar.–Jul.	TESS 2 min	TESS
2018 Nov.–2019 Jan.	CORALIE	24
2018 Nov.–Dec.	FEROS	2
2018 Sep 15	LCO-SAAO	i'
2018 Sep 21	LCO-CTIO 0.4 m	i'
2018 Oct. 07	IRSF	H
2018 Oct. 07	IRSF	J
2018 Oct. 18	MtStuart	g'
2018 Oct. 22	Hazelwood	Ic
2018 Oct. 24	Hazelwood	Ic
2018 Nov. 08	LCO-CTIO	g'
2018 Nov. 08	LCO-CTIO	i'
TOI-169		
2018 Jul. 25–Sep 20	TESS FFI	TESS
2019 Jun.–Jul.	TESS 2 min	TESS
2018 Oct.–Nov.	FEROS	10
2019 Jun.–Jul.	CORALIE	6
2018 Sep. 11	LCO-SAAO	i'
2018 Sep. 26	LCO-SAAO	i'
2018 Oct. 01	CHAT	i'
2018 Nov. 03	Trappist-South	B
2018 Nov. 13	LCO-CTIO	g'

CORALIE is fed by a 2″ fibre and has a resolution of $R = 60\,000$. RVs and line bisector spans were calculated via cross-correlation with a G2 binary mask, using the standard CORALIE data-reduction pipeline.

The three systems were also monitored with the FEROS spectrograph (Kaufer & Pasquini 1998) mounted on the MPG 2.2 m telescope installed at La Silla Observatory. FEROS has a spectral resolution of $R = 48\,000$ and is fibre fed from the telescope. Observations were performed with the simultaneous calibration mode where a second fibre is illuminated by a Thorium-Argon lamp in order to trace the instrumental RV drift. 17, 2, and 10 FEROS spectra were obtained for HIP 65A, TOI-157 and TOI-169, respectively. FEROS data were processed with the CERES pipeline (Brahm et al. 2017), which delivers precision RVs computed via the cross-correlation technique.

The first few RV measurements were used for reconnaissance, to check for a visual or spectroscopic binary. Once a significant change in RV had been identified to be consistent
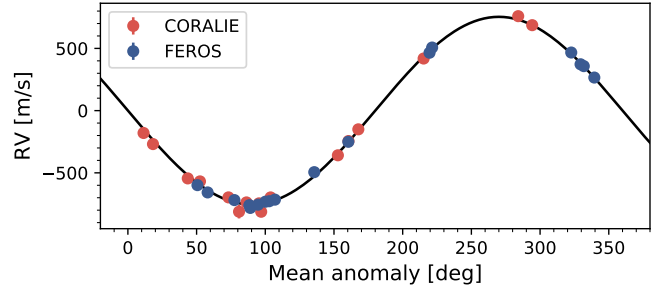
Fig. 1. RVs from CORALIE and FEROS for HIP 65A, phase folded on the ephemeris of the planet. Error bars are included, but too small to show.
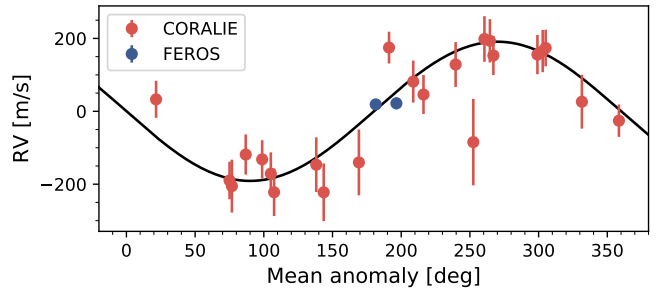
Fig. 2. CORALIE and FEROS RVs for TOI-157, phase folded on the ephemeris for TOI-157b.
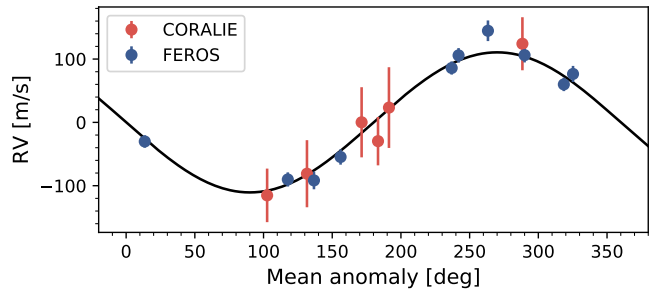
Fig. 3. CORALIE and FEROS RVs for TOI-169, phase folded on the ephemeris for TOI-169b.

with the ephemerides provided by TESS we commenced intensive follow-up observations. The RVs from both CORALIE and FEROS are listed in Appendix A. One CORALIE measurement from BJD 58 460.665537 (−2 400000) was excluded from the global analysis due to low signal-to-noise ratio (S/N). In Figs. 1–3 we plot the phase folded RVs along with our best-fit model from the joint analysis (Sect. 4).

The Lomb-Scargle periodograms for the RV measurements show significant signals (above 0.1% False Alarm Probability, FAP) at the orbital periods recovered from the transit data for all three systems. To ensure that the RV signal does not originate from cool stellar spots or a blended eclipsing binary, we checked for correlations between the line bisector span and the RV measurements (Queloz et al. 2001b). We found no evidence for correlation for any of our targets. None of the Lomb-Scargle periodograms for the activity indicators have peaks above 10% FAP.

2.3. Follow-up photometry

We acquired ground-based time-series follow-up photometry of HIP 65A, TOI-157 and TOI-169 as part of the TESS Follow-up

Observing Program (TFOP) to attempt to (1) rule out nearby eclipsing binaries (NEBs) as potential sources of the TESS detection, (2) detect the transit-like event on target to confirm the event depth and thus the TESS photometric deblending factor, (3) refine the TESS ephemerides, (4) provide additional epochs of transit centre time measurements to supplement the transit timing variation (TTV) analysis, and (5) place constraints on transit depth differences across optical filter bands. We used the `TESS Transit Finder`, which is a customised version of the `Tapir` software package (Jensen 2013), to schedule our transit observations.

2.3.1. Las Cumbres Observatory Global Telescope (LCOGT)

Five, four, and three full transits of HIP 65A, TOI-157 and TOI-169, respectively, were observed using the Las Cumbres Observatory Global Telescope (LCOGT) 1.0-m and 0.4-m network (Brown et al. 2013) nodes at Cerro Tololo Inter-American Observatory (CTIO), Siding Spring Observatory (SSO), and South Africa Astronomical Observatory (SAAO). The 1.0-m telescopes are equipped with 4096 × 4096 LCO SINISTRO cameras having an image scale of $0\farcs389$ pixel^{-1} resulting in a $26' \times 26'$ field of view. The 0.4-m telescopes are equipped with 2048 × 3072 SBIG STX6303 cameras having an image scale of $0\farcs57$ pixel^{-1} resulting in a $19' \times 29'$ field of view. The images were calibrated using the standard LCOGT BANZAI pipeline (McCully et al. 2018). The photometric data were extracted using the `AstroImageJ` (`AIJ`) software package (Collins et al. 2017).

HIP 65A was observed five times using the SSO 1.0-m network node on 2018-Sep-7 in Pan-STARSS z-short band, 2018-Sep-13 in B-band and i'-band, and 2018-Sep-14 in B-band and i'-band. The HIP 65Ab transit was detected on-target using photometric apertures with radius as small as $1\farcs2$. Since the typical stellar FWHM in the images is $2\farcs1$, most of the flux from the closest *Gaia* DR2 neighbour $3\farcs95$ to the north-west, which is 4.4 magnitudes fainter in TESS band, was excluded from the follow-up target star aperture. Thus, all known neighbouring *Gaia* DR2 stars are ruled out as the source of the on-target transit detection.

TOI-157 was observed using the SAAO 1.0-m network node on 2018-Sep-15 in i'-band, two times using the CTIO 1.0-m network node on 2018-Sep-8 in g'-band and i'-band, and one time using the CTIO 0.4-m network node on 2018-Sep-21 in i'-band. The TOI-157 transit was detected on-target using photometric apertures with radius as small as $4\farcs7$, which rules out all known neighbouring *Gaia* DR2 stars as the source of the transit detection.

TOI-169 was observed using the SAAO 1.0-m network node on 2018-Sep.-11 in i'-band, the CTIO 1.0-m network node on 2018-Sep.-13 in g'-band, and the SAAO 0.4-m network node on 2018-Sep.-26 in i'-band. The TOI-169 transit was detected on-target using photometric apertures with radius as small as $2\farcs7$, which rules out all known neighbouring *Gaia* DR2 stars as the source of the transit detection.

2.3.2. Next Generation Transit Survey (NGTS)

Two full transits of HIP 65Ab were observed using the Next Generation Transit Survey (NGTS, Wheatley et al. 2018) on the nights UT 2018-Nov.-30 and 2018-Dec.-02. On both nights, a single 0.2 m NGTS telescope was used. Across the two nights, a total of 2422 images were obtained using the custom NGTS filter (520–890 nm) and an exposure time of 10 s. We had sub-pixel level stability of the target on the CCD, thanks to the telescope guiding performed by the DONUTS algorithm (McCormac et al.

2013). The data reduction was performed using a custom aperture photometry pipeline. For the reduction, comparison stars, which were similar to HIP 65A in both apparent magnitude and colour, were automatically selected.

2.3.3. Chilean-Hungarian Automated Telescope (CHAT)

A full transit of TOI-169 was obtained with the 0.7 m Chilean-Hungarian Automated Telescope (CHAT) installed at Las Campanas Observatory in Chile. The observations took place on the night of 2018-Oct-01, using the sloan i filter and an exposure time of 130 s. The 60 science images where processed with a dedicated pipeline which is an adaptation of the routines developed for the processing of photometric time series with LCOGT facilities (see Hartman et al. 2019; Jordán et al. 2019; Espinoza et al. 2019). This pipeline automatically determines the optimal aperture for the photometry, which was 7 pixels in this case ($4\farcs2$). The obtained per point precision was 1100 ppm, which was enough to detect the ≈6 mmag transit, confirming that this was the source of the signal detected by TESS.

2.3.4. TRAPPIST-South

TRAPPIST-South at ESO-La Silla Observatory in Chile is a 60 cm Ritchey-Chretien telescope, which has a thermoelectrically cooled 2K × 2K FLI Proline CCD camera with a field of view of $22' \times 22'$ and pixel-scale of 0.65 arcsec pixel^{-1} (for more detail, see Jehin et al. 2011; Gillon et al. 2013). We carried out a full-transit observation of TOI-169 on 2018-Nov.-03 with B filter with an exposure time of 50 s. We took 220 images and made use of `AIJ` to perform aperture photometry. The optimum aperture being 7 pixels ($4\farcs55$) and a PSF of $2\farcs80$. We confirmed the event on the target star and we cleared all the stars of eclipsing binaries within 2.5 arcmin around the target star.

2.3.5. Infrared Survey Facility (IRSF)

TOI-157 was observed with the Infrared Survey Facility (IRSF) 1.4 m telescope located in Sutherland, South Africa on UT 2018-Oct-7. We used the Simultaneous Infrared Imager for Unbiased Survey (SIRIUS: Nagayama et al. 2003) camera for the observation, which is equipped with two dichroic mirrors and can take J, H, and K_s bands simultaneously with three 1K×1K HgCdTe detectors. On the observing night, the K_s band detector had a trouble, and only J and H band data were useful. We took 300 frames for each band with an exposure time of 60 s. We used a position locking software introduced in Narita et al. (2013) during the observation. We applied a dedicated pipeline for the SIRIUS data[1] to make sky flats. Dark subtraction, flat fielding, and subsequent standard aperture photometry were done with a customised pipeline by Fukui et al. (2011).

2.3.6. Perth Exoplanet Survey Telescope (PEST)

We observed a full transit of HIP 65Ab on UTC 2018-Sep-14 in V-band from the Perth Exoplanet Survey Telescope (PEST) near Perth, Australia. The 0.3 m telescope is equipped with a 1530 × 1020 SBIG ST-8XME camera with an image scale of $1\farcs2$ pixel^{-1} resulting in a $31' \times 21'$ field of view. A custom pipeline based on `C-Munipack`[2] was used to calibrate the images and extract the

---

[1] http://irsf-software.appspot.com/yas/nakajima/sirius.html
[2] http://c-munipack.sourceforge.net

differential photometry, using an aperture with radius 10″.6. The images have typical stellar point spread functions (PSFs) with a FWHM of $\sim 4''$.

2.3.7. Mt. Stuart Observatory

We observed a full transit of TOI-157 on UTC 2018-Oct-18 in g'-band from Mt. Stuart near Dunedin, New Zealand. The 0.32 m telescope is equipped with a 3072×2048 SBIG STXL6303E camera with an image scale of 0″.88 pixel^{-1} resulting in a $44' \times 30'$ field of view. AIJ was used to calibrate the images and extract the differential photometry with an 8″.8 aperture radius. The images have typical stellar PSFs with a FWHM of ~5″.

2.3.8. Mt. Kent Observatory (MKO)

We observed a full transit of HIP 65Ab on UTC 2018-Sep.-10 in r'-band from Mt. Kent Observatory (MKO) near Toowoomba, Australia. The 0.7-m telescope is equipped with a 4096×4096 Apogee Alta F16 camera with an image scale of 0″.41 pixel^{-1} resulting in a $27' \times 27'$ field of view. AIJ was used to calibrate the images and extract the differential photometry with a 3″.3 aperture radius. The images have typical stellar PSFs with a FWHM of ~2″.

2.3.9. Hazelwood Observatory

Hazelwood Observatory is a backyard observatory located in Victoria, Australia. Photometric follow-up data for TOI-157 was obtained on 2018-Oct.-22 and 24 in the Ic band, using a 0.32-m Planewave CDK telescope and SBIG STT3200 CCD camera, with 2148×1472 pixels (FoV $20' \times 13'$). The observations on 2018-Oct.-22 covered a full transit with some observations missing near ingress and at mid-transit due to passing cirrus cloud. The observations taken on 2018-Oct.-24 were not continuous due to passing cirrus cloud. The frames were corrected for Bias, Dark and Flat Fields using MaximDL. Differential photometry was extracted using AIJ.

2.4. SOAR speckle imaging

TESS is in-sensitive to close companions due to its relatively large 21″pixels. Companion stars can contaminate the photometry, resulting in an underestimated planetary radius or may be the source of an astrophysical false positive. We searched for previously unknown companions to HIP 65A, TOI-157 and TOI-169 with SOAR speckle imaging (Tokovinin 2018) on UT 2018-Sep.-25 and UT 2018-Oct.-21, observing in a similar visible bandpass as TESS. Further details of the observations are available in Ziegler et al. (2020). We did not detect any nearby stars to the three host stars within 3″. The 5σ detection sensitivity and the speckle auto-correlation function from the SOAR observations are plotted in Fig. 4.

3. Spectral analysis

Stellar atmospheric parameters, including effective temperature, T_{eff}, surface gravity, $\log g$, and metalicity, [Fe/H], were derived using SPECMATCH-EMP (Yee et al. 2017) on stacked FEROS spectra for HIP 65A and TOI-169. For TOI-157, we ran SPECMATCH-EMP on stacked CORALIE spectra.

SPECMATCH-EMP matches the input spectra to a vast library of stars with well-determined parameters derived with a variety of independent methods, such as interferometry, optical and
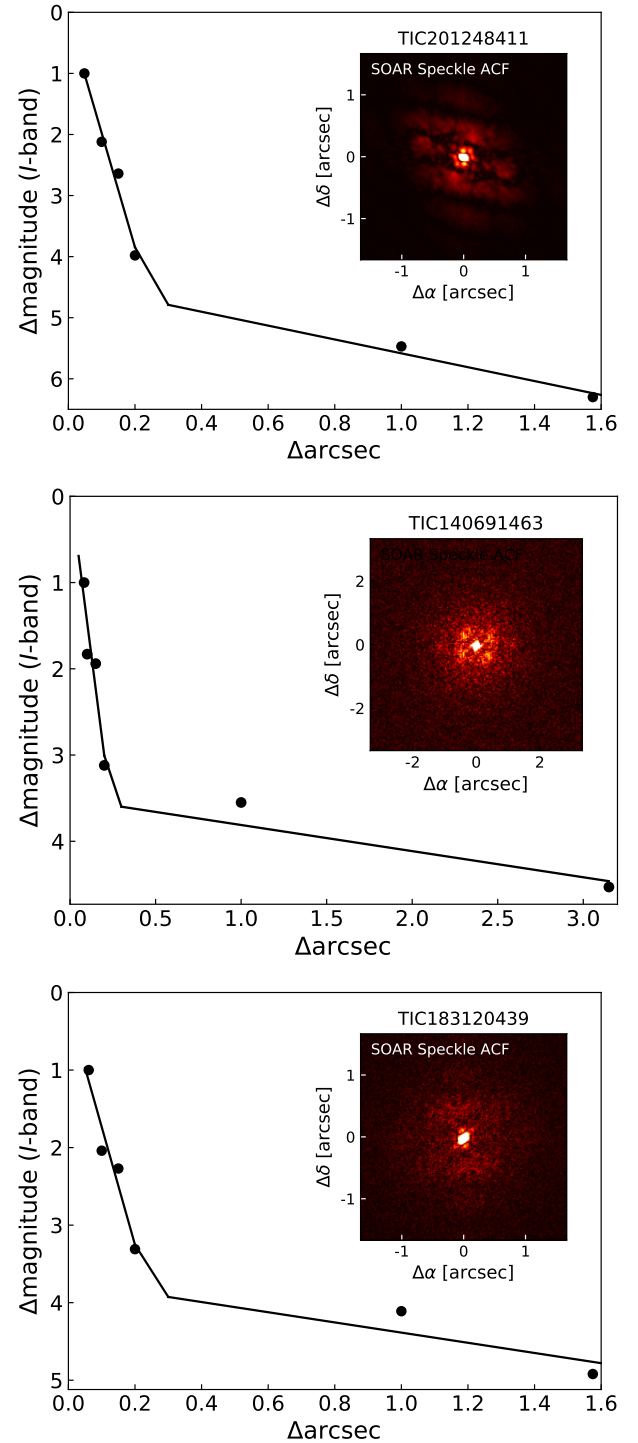

Fig. 4. SOAR speckle imaging of HIP 65A, TOI-157, and TOI-169 from the top.

NIR photometry, asteroseismology, and LTE analysis of high-resolution optical spectra. We used the spectral region around the Mg I b triplet (5100–5340 Å) to match our spectrum to the library spectra through χ^2 minimisation. A weighted linear combination of the five best matching spectra were used to extract T_{eff}, R_s and [Fe/H].

The projected rotational velocity of the star, $v \sin i$, was computed using the calibration between $v \sin i$ and the width of the CORALIE CCF from Santos et al. (2002). The formal result was smaller than what can be resolved by CORALIE, and we

Table 3. Median values and 68% confidence intervals of the posterior distributions from joint modelling for HIP 65A, TOI-157, and TOI-169 as as described in Sect. 4.

| Stellar parameters:		HIP 65A	TOI-157	TOI-169
M_*	Mass ($M_\odot$)	0.781 ± 0.027	$0.948^{+0.023}_{-0.018}$	$1.147^{+0.069}_{-0.075}$
R_*	Radius ($R_\odot$)	$0.7242^{+0.0081}_{-0.0091}$	$1.167^{+0.017}_{-0.014}$	$1.288^{+0.020}_{-0.019}$
L_*	Luminosity ($L_\odot$)	$0.2099^{+0.0077}_{-0.0084}$	$1.047^{+0.055}_{-0.049}$	$1.789^{+0.066}_{-0.061}$
ρ_*	Density (cgs)	$2.898^{+0.085}_{-0.074}$	$0.842^{+0.029}_{-0.030}$	$0.756^{+0.060}_{-0.061}$
$\log g$	Surface gravity (cgs)	$4.611^{+0.011}_{-0.010}$	4.281 ± 0.011	$4.278^{+0.029}_{-0.033}$
$T_{\rm eff}$	Effective temperature (K)	4590 ± 49	5404^{+70}_{-67}	5880^{+54}_{-49}
[Fe/H]	Metallicity (dex)	0.18 ± 0.08	0.24 ± 0.09	0.24 ± 0.09
Age	Age (Gyr)	$4.1^{+4.3}_{-2.8}$	$12.82^{+0.73}_{-1.4}$	$4.7^{+2.7}_{-2.0}$
A_V	V-band extinction (mag)	0.02 ± 0.01	0.12 ± 0.08	$0.04^{+0.05}_{-0.03}$
d	Distance (pc)	61.89 ± 0.08	$362.1^{+2.9}_{-2.8}$	$412.5^{+4.3}_{-4.2}$
$v \sin i$	Projected rotational velocity (km s^{-1})	<2.5	<2.5	<2.5
$P_{\rm rot}$	Rotational period (days)	$13.2^{+1.9}_{-1.4}$		
$\log R'_{\rm HK}$	Ca H&K chromospheric index (dex)	-4.54 ± 0.03	-4.7 ± 0.2	-5.0 ± 0.3
Planetary parameters:		HIP 65Ab	TOI-157b	TOI-169b
$R_{\rm P}$	Radius ($R_{\rm J}$)	$2.03^{+0.61}_{-0.49}$	$1.286^{+0.023}_{-0.020}$	$1.086^{+0.081}_{-0.048}$
$M_{\rm P}$	Mass ($M_{\rm J}$)	3.213 ± 0.078	$1.18^{+0.13}_{-0.12}$	$0.791^{+0.064}_{-0.060}$
P	Period (days)	0.9809734 ± 0.0000031	2.0845435 ± 0.0000023	2.2554477 ± 0.0000063
$T_{\rm C}$	Time of conjunction (BJD$_{\rm TDB}$)	58326.10418 ± 0.00011	$58326.54771^{+0.00022}_{-0.00021}$	$58327.44174^{+0.00065}_{-0.00066}$
a	Semi-major axis (AU)	$0.01782^{+0.00020}_{-0.00021}$	$0.03138^{+0.00025}_{-0.00020}$	$0.03524^{+0.00069}_{-0.00079}$
i	Inclination (Degrees)	$77.18^{+0.92}_{-1.00}$	$82.01^{+0.15}_{-0.16}$	$80.98^{+0.31}_{-0.38}$
b	Transit impact parameter	$1.169^{+0.095}_{-0.077}$	$0.8045^{+0.0069}_{-0.0068}$	$0.9221^{+0.014}_{-0.0098}$
e	Orbital eccentricity	0 (adopted, $2\sigma < 0.02$)	0 (adopted, $2\sigma < 0.21$)	0 (adopted, $2\sigma < 0.12$)
K	RV semi-amplitude (m s^{-1})	753.7 ± 5.0	192 ± 20	$110.5^{+7.6}_{-6.9}$
$T_{\rm eq}$	Equilibrium temperature (K)	1411 ± 15	1588^{+21}_{-20}	1715^{+22}_{-20}
$R_{\rm P}/R_*$	Radius of planet in stellar radii	$0.287^{+0.088}_{-0.068}$	$0.11329^{+0.00056}_{-0.00054}$	$0.0866^{+0.0056}_{-0.0031}$
a/R_*	Semi-major axis in stellar radii	$5.289^{+0.051}_{-0.045}$	$5.785^{+0.066}_{-0.069}$	$5.88^{+0.15}_{-0.16}$
δ	Transit depth (fraction)	$0.082^{+0.058}_{-0.034}$	$0.01283^{+0.00013}_{-0.00012}$	$0.00750^{+0.0010}_{-0.00053}$
Depth	Flux decrement at mid transit	0.01094 ± 0.00033	$0.01283^{+0.00013}_{-0.00012}$	$0.00733^{+0.00036}_{-0.00037}$
τ	Ingress/egress transit duration (days)	$0.01637^{+0.00013}_{-0.00012}$	$0.02309^{+0.00083}_{-0.00076}$	$0.03531^{+0.00077}_{-0.0050}$
T_{14}	Total transit duration (days)	0.03274 ± 0.00025	$0.08941^{+0.00055}_{-0.00052}$	0.0711 ± 0.0012
$T_{\rm FWHM}$	FWHM transit duration (days)	$0.01637^{+0.00013}_{-0.00012}$	$0.06631^{+0.00065}_{-0.00067}$	$0.03587^{+0.0048}_{-0.00076}$
$\rho_{\rm P}$	Density (cgs)	$0.48^{+0.61}_{-0.26}$	$0.686^{+0.080}_{-0.078}$	$0.76^{+0.14}_{-0.17}$
$\log g_{\rm P}$	Surface gravity	$3.29^{+0.24}_{-0.23}$	$3.247^{+0.046}_{-0.050}$	$3.219^{+0.058}_{-0.079}$
Θ	Safronov number	$0.072^{+0.022}_{-0.017}$	$0.0606^{+0.0065}_{-0.0064}$	$0.0445^{+0.0039}_{-0.0041}$
$\langle F \rangle$	Incident flux (10^9 erg s^{-1} cm^{-2})	$0.899^{+0.038}_{-0.039}$	$1.446^{+0.077}_{-0.070}$	$1.964^{+0.10}_{-0.090}$

Notes. $P_{\rm rot}$, $v \sin i$ and $\log R'_{\rm HK}$ are results from separate analyses, see Sects. 3 and 5.1.

can therefore only establish an upper limit of 2.5 km s^{-1}. An independent analysis performed on the FEROS spectra using the CERES pipeline yields similar $v \sin i$ upper limits.

Chromospheric activity indicators $\log R'_{\rm HK}$ were computed for each of the three stars using the FEROS spectra using the prescription in Boisse et al. (2009). The average values are listed in Table 3.

4. Joint analysis of transit light curves and RVs

The planetary and stellar parameters for the three systems were modelled jointly and self-consistently using the TESS discovery light curves, follow-up photometry and RV measurements from FEROS and CORALIE. We use the most recent version of *EXOFASTv2* (Eastman et al. 2019, 2013), which can fit any
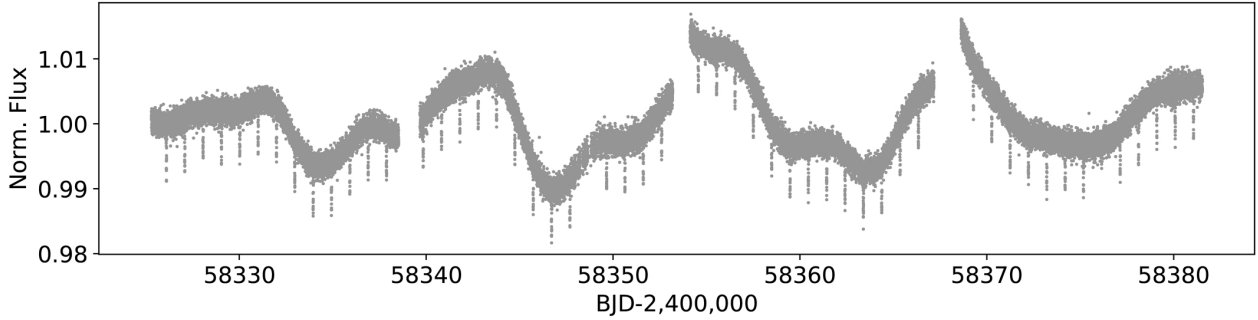
Fig. 5. TESS 2-min cadence data for HIP 65A spanning Sectors 1 and 2. The stellar rotational period of $13.2^{+1.9}_{-1.4}$ days clearly shows up in the PDC-SAP flux. The light curve was flattened while masking the transits before modelling the transits.

number of transits and RV sources while exploring the vast parameter space through a differential evolution Markov chain coupled with a Metropolis-Hastings Monte Carlo sampler. Built-in Gelman-Rubin statistic (Gelman & Rubin 1992; Gelman et al. 2003; Ford 2006) is used to check the convergence of the chains. We ran *EXOFASTv2* until convergence, and discarded the first chains which have χ^2 above the median χ^2 as the "burn-in" phase, not to bias the final posterior distributions towards the starting point.

At each step in the MCMC, we evaluate the stellar properties and limb darkening coefficients by interpolating tables from Claret & Bloemen (2011). The analytic expressions from Mandel & Agol (2002) are used for the transit model and a standard single Keplerian orbit for the RV signal. Four parameters are fitted for the star $T_{\rm eff}$, [Fe/H], $\log M_*$ and R_*. We applied Gaussian priors on $T_{\rm eff}$ and [Fe/H] from the spectral analysis, presented in Sect. 3. Stellar density is determined from the transit light curve. The *Gaia* DR2 parallax was used along with SED-fitting of the broad band photometry presented in Table 1 to constrain the stellar radius further. We set an upper limit on the *V*-band extinction from Schlegel et al. (1998) and Schlafly & Finkbeiner (2011), to account for reddening along the line of sight. Combining all this information allows us to perform detailed modelling of the star with the Mesa Isochrones and Stellar Tracks (MIST Dotter 2016; Choi et al. 2016).

When modelling RVs and transit photometry simultaneously, each planet has five free parameters (assuming a circular orbit) and two additional RV terms for each instrument (CORALIE & FEROS) for the systemic velocity and RV-jitter. For the transit light curves a set of two limb darkening coefficients for each photometric bands are fitted along with the base line flux and variance of the light curve. The TESS PDC-SAP and FFI data were modelled separately to account for different error-properties. For all three planets presented in this study, the precision in the follow-up light-curves is not high enough to detect depth variation as a function of wavelength caused by planetary atmospheric absorption. For the final set of adopted parameters, we fitted one consistent model to all the data which has a fixed transit depth across wavelength.

To avoid Lucy-Sweeney bias of the eccentricity measurement (Lucy & Sweeney 1971) we constrain the orbital eccentricity to be zero. To test for possible non-circular orbits, we run a separate MCMC with no constraint on the eccentricity. The data for HIP 65Ab, TOI-157b, and TOI-169b are all consistent with circular orbits. We adopt median values of the posterior distributions and 68% confidence intervals for the models with eccentricity fixed to zero as the final parameters presented in Table 3, while quoting the 2σ upper limit of the eccentricity.

HIP 65 A has a star 3.95″ away which was not corrected for in the TESS light curve. It was also not spatially resolved in the ground-based follow-up photometry. We account for this blending by fitting a dilution parameter for each photometric band, as detailed in Sect. 5.2.

5. Multi faceted analysis of the HIP 65 system

HIP 65Ab is an USP Jupiter near the Roche Lobe limit in a binary system and requires an extensive analysis which we present here.

5.1. Stellar rotation and activity for HIP 65A

The PDC-SAP light curve for HIP 65A shows significant stellar variability attributed to star spots coming in and out of view as the star rotates, see Fig. 5. Using a Lomb-Scargle periodogram we find a rotation period of $P_{\rm rot} = 13.2^{+1.9}_{-1.4}$ days. This is in good agreement with the predicted period from $\log R'_{\rm HK}$ derived in Sect. 3 when using the calibrations from Suárez Mascareño et al. (2015). We find a peak-to-peak variation of about 2% which corresponds to a minimum star spot filling factor of ∼3% of the stellar disc when assuming a sun-like luminosity contrast between spot and continuum as prescribed in Bonomo & Lanza (2012) and Morris et al. (2017a).

For the transit analysis presented in Sect. 4 we flatten the light curve by fitting third order polynomials to chunks of the light curve while masking the transits. This type of spline filtering acts as a simple low pass filter (see e.g. Armstrong et al. 2016). The presence of star spots can affect the radius estimate of transiting planets: (1) as the planet crosses a star spot and the transit shape is thus distorted while the depth is underestimated. (2) the deficit in flux induced by the presence of a cold star spot increases the relative flux blocked by the transiting planet. The later effect leads to an overestimation of the planetary radius. Both of these mechanisms are demonstrated for instance on CoRoT-2 by Wolter et al. (2009). For HIP 65Ab these effects are negligible as the uncertainty on the planet radius is dominated by the degeneracy between orbital inclination and planetary radius introduced by the grazing transit configuration. Visual inspection of the transit light curve residuals does not indicate any spot crossing events.

The expected impact of stellar activity for a K-star with $P_{\rm rot} = 13.2$ days on the RVs is of the order of ∼10 m s^{-1} (Suárez Mascareño et al. 2017, 2015). This is comparable to the uncertainty on the FEROS RVs and much smaller than the uncertainties of the CORALIE data. We find no correlation between RV-residuals to the best-fit model and stellar activity indicators,
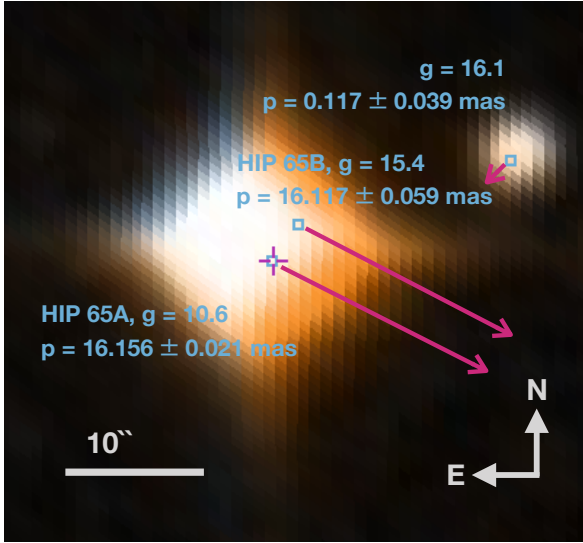
Fig. 6. Multi-colour Digitized Sky Survey image of HIP 65A (centre cross-hair) and the nearby companion HIP 65B separated by 3.95″ towards north. Their common proper motions are indicated as pink arrows. Blue squares are *Gaia* DR2 sources in the field, with *Gaia* magnitudes and parallaxes denoted.

such as bisector span, FWHM of the CCF, $H\alpha$-index. None of the respective Lomb-Scargle periodograms have peaks above 10% FAP. We do thus not perform any correction for stellar activity.

5.2. Stellar companion to HIP 65A

HIP 65A is part of a visual binary separated by 3.95″ on the sky. The two stars are associated with similar proper motion and parallax (Gaia Collaboration 2018), as illustrated in Fig. 6. We denoted them HIP 65A and HIP 65B. Their angular separation on sky corresponds to 245 AU. HIP 65B is a M-dwarf with $T_{\rm eff} = 3713^{+994}_{-290}$ K according to *Gaia* DR2. The work by Anders et al. (2019) presents more detailed modelling of *Gaia* stars including HIP 65B. They present a refined effective temperature of 3861^{+183}_{-259} K and mass of $0.30^{+0.003}_{-0.05}$ $M_\odot$. Table 4 summarises the fundamental properties of HIP 65B.

The blending effect from the HIP 65B star was not taken into account when producing the PDC-SAP light curve, as the star was not included in the TESS input catalog version 7 (TICv7, Stassun et al. 2018) which was used to correct the normalised light curve for dilution. TICv8 (Stassun et al. 2019) does include HIP 65B which has $T = 14.30$ mag, which means it is fainter than HIP 65A by $\Delta T = 4.4$ mag. The effect of dilution is small, but non-negligible. Therefore we fitted dilution parameters for this target in all photometric bands, assuming all follow-up light curves include light from both stars. For the TESS band we use the TESS magnitude to compute the dilution factor. For the photometric bands in which the follow-up light curves were taken we use the *Tycho V*-band magnitude along with expected magnitude differences from Pecaut & Mamajek (2013) for a star with the given $T_{\rm eff}$.

5.3. Orbital analysis of HIP 65A and HIP 65B using Gaia

Gaia DR2 measured precise positions and proper motions for HIP 65A and HIP 65B, so we derived orbital element constraints from these measurements using the Linear Orbits for the Impatient algorithm (LOFTI, Pearce et al. 2020). LOFTI

Table 4. Stellar properties for HIP 65B, companion to HIP 65A.

Property	HIP 65B	Source
2MASS ID	None, blended w. HIP 65A	2MASS
Gaia ID DR2	4923860051276772480	*Gaia*
TIC ID	616112169	TESS
Astrometric properties		
RA	00:00:44.28	TESS
Dec	−54:49:47.94	TESS
$\mu_{\rm RA}$ (mas yr^{-1})	−207.466 ± 0.086	*Gaia*
$\mu_{\rm Dec}$ (mas yr^{-1})	−72.266 ± 0.081	*Gaia*
Parallax (mas)	16.117 ± 0.059	*Gaia*
Distance (pc)	61.94 ± 0.23	
Photometric properties		
V (mag)	16.55 ± 0.07	[†]
G (mag)	15.3877 ± 0.0008	*Gaia*
T (mag)	14.30 ± 0.014	TESS

Notes. [†] V-band magnitude from Knapp & Nanson (2018).
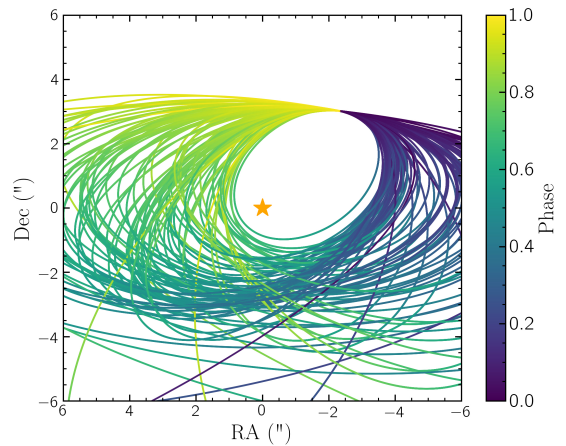
Fig. 7. Selection of 100 orbits from the posterior sample of the fit of HIP65B relative to HIP65A using *Gaia* positions and proper motions. Inclination consistent with HIP65Ab is absent from our posteriors, and low eccentricities are preferred.

uses rejection sampling to determine orbital element posterior probability distributions for stellar binaries derived from *Gaia* DR2 positions and proper motions. We ran LOFTI on the relative *Gaia* measurements for HIP 65B relative to HIP 65A until the rejection sampling algorithm had accepted 50 000 orbits, comprising our posterior orbit sample.

The *Gaia* measurements for the pair are not precise enough to constrain the orbital elements to a high degree, as illustrated in Fig. 7. Additionally, HIP 65B has a slightly elevated Renormalised Unit Weight Error (RUWE) of 1.28, whereas RUWE < 1.2 indicates a well-behaved *Gaia* astrometric solution (Lindegren et al. 2018), so the assumption of a pair of single stars on a Keplerian orbit may not be appropriate. Nevertheless, our results provide some meaningful limits on the orbital architecture of the system, as presented in Table 5. We find inclinations $109.2° < i < 161.9°$ comprise the majority of the posterior, making edge-on inclination consistent with HIP 65Ab highly unlikely. Low eccentricity ($e < 0.5$) and periastron > 75 AU orbits are preferred.

Table 5. Orbital parameter posterior distributions for HIP 65A and HIP 65B from *Gaia* astrometry.

Parameter [a]	Median	Mode	68% Min CI [b]	95% Min CI
$\log{}^{(a)}$ (AU)	2.43	2.42	(2.19, 2.51)	(2.18, 2.82)
e	0.31	0.08	(0, 0.49)	(0, 0.67)
i ($\circ$) [c]	126.4	125.0	(113.6, 136.5)	(109.2, 161.9)
ω ($\circ$)	178.4	316.2	(119.0, 341.8)	(17.9, 360.0)
Ω ($\circ$) [d]	104.4	90.0	(78.6, 135.1)	(29.6, 178.4)
T_0 (yr)	806.6	1319.6	(-383.7, 1564.9)	(-7192.1, 2013.9)
$\log[a\,(1-e)]$	2.30	2.42	(1.89, 2.49)	(1.73, 2.71)

Notes. [a]Orbital parameters: semi-major axis (a), eccentricity (e), inclination (i), argument of periastron (ω), longitude of nodes (Ω), epoch of periastron passage (T_0), and periastron distance [$a\,(1-e)$]. [b]Posterior distributions are not Gaussian, so we report the 68 and 95% minimum credible intervals. [c]Inclination is defined relative to the plane of the sky, $i = 90°$ is edge-on. [d]In the absence of radial velocity information, there is a degeneracy between ω and Ω, so we limit Ω to be on the interval [0, 180]. If in the future radial velocity is obtained and $\Omega > 180°$, 180° should be added to both Ω and ω.
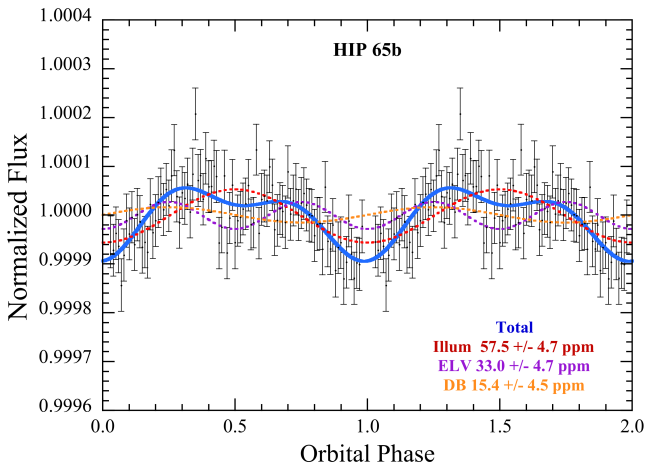
Fig. 8. Out-of-transit folded and binned TESS light curve for HIP 65Ab. The red, purple, and orange curves are sinusoids meant to represent the illumination, ellipsoidal light variations, and Doppler boosting effects, respectively (see text for details). The blue curve is the sum of these and represents the best fit of this model to the out-of-transit light curve.

5.4. Phase curve analysis for HIP 65Ab

A TESS phase folded light curve of HIP 65Ab is shown in Fig. 8 with the eclipses removed. The data are phase-folded with the orbital period and averaged into 100 bins that are ∼14 min long, each with the contributions of about 350 individual flux measurements. For the individual flux measurements, we measure an rms scatter in the data points of ≃980 ppm, and thus the statistical uncertainty in each bin of the light curve is approximately 53 ppm. A casual inspection shows that the light curve exhibits a characteristic orbital phase curve as it has been possible to detect for exoplanets since the CoRoT space-mission (Snellen et al. 2009; Mazeh & Faigler 2010).

We fitted sines and cosines of ωt and $2\omega t$ to the out-of-transit light curve, where ω is the angular frequency of the orbit, to represent various physical effects (see e.g. van Kerkwijk et al. 2010; Carter et al. 2011; Shporer 2017; Niraula et al. 2018; Shporer et al. 2019). We limited ourselves to just these four terms given the limited statistics in our folded out-of-eclipse light curve. The red curve in Fig. 8 is the $\cos \omega t$ term representing the illumination effect of the host star on the planet; the purple curve is the $\cos 2\omega t$ term to approximate the bulk of the ellipsoidal variations ("ELVs"); and the orange curve is the $\sin \omega t$ term for

the Doppler boosting effect (Loeb & Gaudi 2003; van Kerkwijk et al. 2010). The three terms were detected at the 12, 7, and 3.4 σ confidence levels, respectively, and there was no statistically significant amplitude for a $\sin 2\omega t$ term, where no physical effect is expected.

We next utilised the amplitudes of the ELV and Doppler boosting terms to make an independent determination of the planetary mass. Following the expressions and references in Shporer et al. (2019) we adopted a Doppler boosting coefficient in front of the $K_{RV}/c \sin i$ term of $4.2^{+1.8}_{-1.2}$ and an ELV coefficient in front of the $q(R_p/a)^3 \sin^2 i$ term of 1.25 ± 0.25, where K_{RV} is the orbital RV semi-amplitude of the host star, q the planet to host star mass ratio, and a is the orbital radius of the planet. Since we know the mass of the host star and the orbital inclination to ∼1°, either the Doppler boosting or ELV measurement, in principle, determines the planetary mass. We therefore carried out a Monte Carlo evaluation of the overall uncertainty in the planet mass using both measurements (Joss & Rappaport 1984). From this analysis we find $M_p = 3.4 \pm 0.6\ M_J$, which is in agreement with RV-derived mass of $3.213 \pm 0.078\ M_J$.

Finally, in regard to the out-of-transit light curve of HIP 65Ab, we explored what we can learn from the illumination term which has an amplitude of 57 ppm. Because the estimated equilibrium temperature of the planet at the sub-stellar point is likely ≲1400 K, we neglect any contribution from the thermal emission of absorbed and reprocessed radiation from the host star. We find that if the Bond albedo of the facing hemisphere of the planet is allowed to be in the range of 0−0.5, then the resultant likelihood distribution of planet radii, as inferred from the illumination term, is close to 1 R_J. On the other hand, if the geometric albedo is constrained to be ≲0.1, then the peak of the radius distribution is close to our transit-based estimate of 2 R_J. This low albedo is quite consistent with the results found recently for WASP-18b (Shporer et al. 2019).

6. Results and discussion

For each system we list the final stellar and planetary parameters in Table 3 with 1σ errors. Figures B.1 through 3 show the final joint model fitted to the discovery and follow-up data.

6.1. HIP 65Ab

HIP 65Ab is an ultra short period ($P = 0.98$ days) Jupiter with mass $3.213 \pm 0.078\ M_J$. Its radius, $R = 2.03^{+0.61}_{-0.49}\ R_J$, is
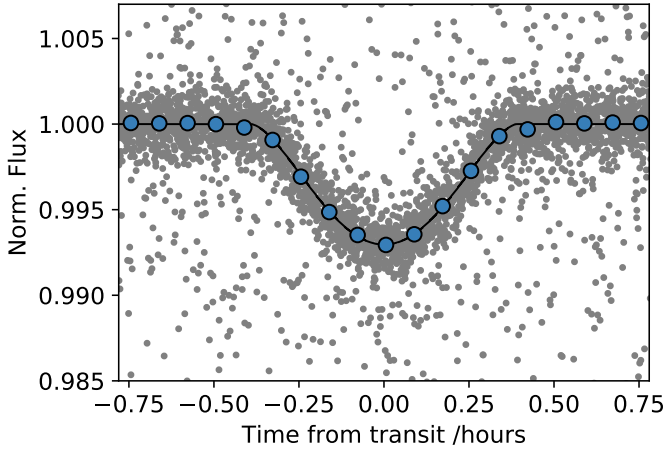
Fig. 9. Phase folded transit light curve for HIP 65Ab including data from two TESS Sectors (see Fig. 5 for the full TESS light curve) and ground based follow-up photometry. Individual follow-up light curves are shown in Fig. B.1. Grey points are the un-binned data. The points with large scatter come from the NGTS 10 sec cadence observations. In blue are the data binned to 5 min in phase space.

poorly constrained as the transit is extremely grazing with impact parameter $b = 1.169^{+0.095}_{-0.077}$. The planet is thus barely transiting with less than half its disc covering the host star during transit. Determining the stellar limb darkening is especially important for a grazing transit where the planet never leaves the limb. In the case of HIP 65A we derive linear and quadratic limb-darkening coefficients $u_1 = 0.545 \pm 0.037$ and $u_2 = 0.195 \pm 0.041$ for the TESS band. The main source of the uncertainty on the planetary radius is the degeneracy between the orbital inclination of the planet and its radius.

The V-shaped, relatively shallow, transit model can be seen in Figs. B.1 and 9 plotted along with the follow-up light curves and TESS data. Figure 3 shows the phase folded RVs showing the large semi-amplitude of 754 ± 5 m s^{-1}.

HIP 65A is a bright ($V = 11.1$) main sequence K-star with $T_{\text{eff}} = 4590 \pm 49$ K, $R_* = 0.724 \pm 0.009\ R_\odot$ and $M_* = 0.781 \pm 0.027\ M_\odot$. We find clear signs of stellar rotation in the TESS light curve corresponding to a rotation period of $P_{\text{rot}} = 13.2^{+1.9}_{-1.4}$ days. The peak-to-peak modulation of the light curve is consistent with a 3% minimum filling factor of star spots on the stellar surface of HIP 65A. This is much higher than for our own Sun, but consistent with other active K-dwarfs, such as the canonical planet host HD 189733 (Sing et al. 2011). For moderately rotating main sequence K- and G-stars we expect spots to be located towards the equator of the star (Schuessler et al. 1996). The lack of star spot crossings seen in our data could be indicating that HIP 65Ab transits one of the stellar poles in a co-planar orbit.

HIP 65A has an associated stellar companion, HIP 65B, separated by 3.95″ with similar distance and proper motion. Based on *Gaia* DR2 data we conclude that HIP 65B is an M-dwarf separated by 269 AU. With such a separation and high mass ratio $q = 0.38$ the protoplanetary disc is not expected to be affected by the presence of the stellar companion (Artymowicz & Lubow 1994; Patience et al. 2008).

The orbital analysis of HIP 65A+B using *Gaia* measurements indicates that the mutual inclination is less than 0.5. This still includes orbital solutions where the Lidov-Kozai mechanism is invoked, which could be used to explain the architecture of the system (Lidov 1962; Kozai 1962). A requirement for such
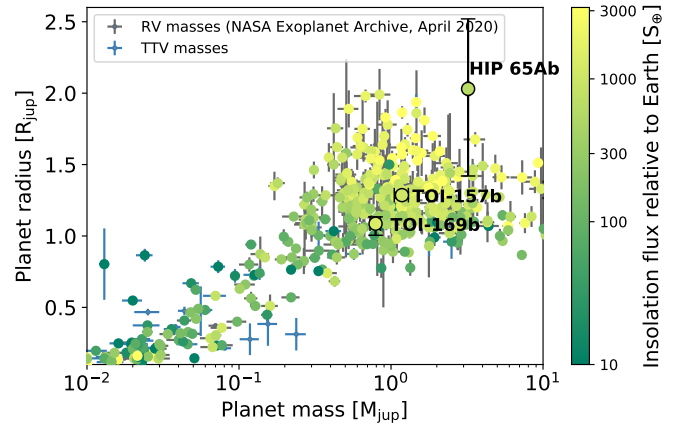
Fig. 10. Mass and radius for known exoplanets extracted from NASA Exoplanet Archive. Only planets with 20% precision on their mass are included. HIP 65Ab, TOI-157b, and TOI-169b are plotted in blue.

a process to occur is that the mutual inclination between the two orbits at high period ratio is large enough. From then, the angular momentum exchange between the two orbits will induce phase-opposed oscillations of the eccentricity and inclination of the inner orbit. At high eccentricity phases, tidal dissipation will take place during the periastron passages, leading the orbit of the planet to shrink. This mechanism was already successfully introduced to explain the observations of planets in binary systems (e.g. Wu & Murray 2003; Fabrycky & Tremaine 2007).

Measuring the spin-orbit misalignment between the central star and the inner planet could help at selecting the mechanism responsible for the current architecture of the system. If a significant misalignment is found, the Lidov-Kozai mechanism will be favoured. If, on the other hand, the spin axis of the star is aligned with the normal to the inner orbit, then the Lidov-Kozai mechanism will be excluded because the planet would not have been misaligned from its original orbit.

Figure 10 shows mass and radius for known exoplanets with HIP 65Ab, TOI-157b, and TOI-169b over-plotted in blue. HIP 65Ab does appear to have an unusually large radius which most likely is overestimated due to the grazing nature of the transit. Close-in gas planets are found to be inflated, as the proximity to the host star can inhibit thermal contraction (Baraffe et al. 2010; Batygin & Stevenson 2010). As seen in Fig. 11 HIP 65Ab receives 642 times more insolation flux than that of the Earth. Given the mass and insolation flux it is unlikely that HIP 65Ab is larger than 1.5 R_J.

The effects of the large planetary mass and radius, relative to the host star, are evident in the TESS light curve. Our analysis of the phase curve yields an illumination effect amplitude of 57.5 ± 4.7 ppm, ELV amplitude 30.0 ± 4.7 ppm, as well as Doppler boosting effect 15.4 ± 4.5 ppm. The mass derived on the basis of the two latter terms is $3.4 \pm 0.6\ M_J$, in agreement with the independently derived RV-mass. We estimate the geometric Bond albedo to be $\lesssim 0.1$, but cannot constrain it further due to large uncertainties on the radius. A study by Wong et al. (2020) presents a systematic phase curve analysis of TOIs for the first year of TESS operation, which are in agreement with our results.

The tidal interaction between HIP 65Ab and its host star is expected to spin up the stellar rotation while removing angular momentum from the orbit. Over time the orbit will circularise and the planet will spiral within the Roche limit of HIP 65A and
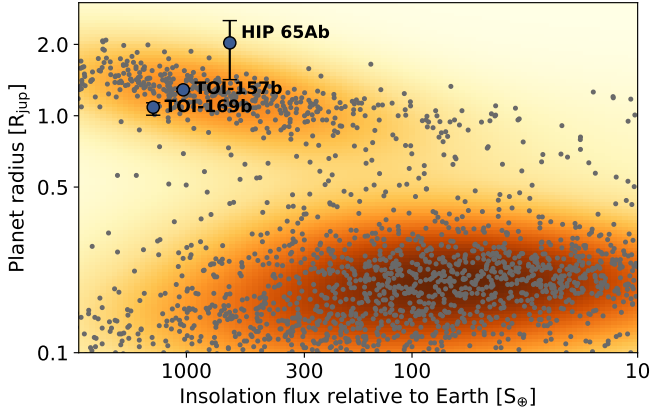
Fig. 11. Insolation flux relative to Earth plotted against radii for known exoplanets extracted from NASA Exoplanet Archive. The orange contours indicate point density (not occurrence) HIP 65Ab, TOI-157b, and TOI-169b are plotted in blue.

Fig. 12. *Top panel*: orbital separation in units of Roche limit as a function of the planet-to-star mass ratio for the planets as in Fig. 10. The symbols sizes are proportional to the planer radius and the colour-coding represents t_{remain} when assuming $Q'_s = 10^7$. The open grey circle is HIP 65Ab when assuming a radius of 1.5 R_J. Filled grey circles are planets with mass <0.1 M_J, which are excluded from the histogram in the bottom panel. *Bottom panel*: distribution of a/a_{Roche} for a subset of the planets from the top and Fig. 10 with masses above 0.1 M_J. The green histogram shows the raw count of planets in bins of 0.2. The solid line is the same distribution but weighted by the inverse of the transit probability for each planet.

disintegrate. We compute the Roche limit, a_{Roche}, as defined for a infinitely compressible object in Faber et al. (2005):

$$a_{Roche} = 2.16 R_p \left(\frac{M_s}{M_p}\right)^{1/3}, \qquad (1)$$

where R_p and M_p are the planet radius and mass respectively and M_s the stellar mass. The Roche limit for HIP 65Ab is 0.013 AU when using using the values listed in Table 3. If using the more realistic planet radius of 1.5 R_J the resulting Roche limit is 0.010 AU. This means that HIP 65Ab is orbiting its host star at a distance corresponding to less than twice the Roche limit.

The efficiency of the tidal dampening is given by the stellar reduced tidal quality factor $Q'_s \equiv 3/2 \, Q_s/k_2$, where Q_s is the tidal quality factor and k_2 the second-order potential Love number. Q'_s can vary from 10^5 to 10^9 and depends on stellar properties which will change throughout the lifetime of the system (Ogilvie & Lin 2007; Damiani & Díaz 2016; Penev et al. 2018).

We calculated the remaining lifetime t_{remain} of the planet using the prescription for slowly rotating stars in Brown et al. (2011):

$$t_{remain} = \frac{2Q'_s}{17n} \frac{M_s}{M_p} \left(\frac{a}{R_s}\right)^5, \; n = \sqrt{\frac{G(M_s + M_p)}{a^3}}, \qquad (2)$$

where a is the semi-major axis of the planetary orbit and R_s the stellar radius. For HIP 65Ab t_{remain} is 76 Myr when using $Q'_s = 10^7$ and 7.6 Gyr for $Q'_s = 10^9$. This is much shorter than the expected age derived from the global modelling using MIST, $4.1^{+4.3}_{-2.8}$ Gyr.

Gyrochronology yields an age of $0.32^{+0.1}_{-0.06}$ Gyr (Barnes 2007). The discrepancy between the two age estimates indicates that the star has been spun up, making the approach of gyrochronology unfeasible. In order to get a life span of the system that is consistent with the MIST age one must use $Q'_s > 10^8$. Other systems with short period planets, such as HAT-P-11b (Bakos et al. 2010), show evidence of tidal spin which induces increased stellar activity (Morris et al. 2017b).

Figure 12 shows the orbital separation of known exoplanets normalised with the Roche limit as a function of planet-to-star mass ratio. The symbol sizes are proportional to the planet radius and the colour-coding represents t_{remain} when assuming $Q'_s = 10^7$. HIP 65Ab is bordering the empty parameter

space representing massive planets close to the Roche limit. The dearth of targets could be the consequence of Jupiters spiralling into their host star (Collier Cameron & Jardine 2018). The bottom panel shows a histogram of the orbital separation in units of a_{Roche}, for giant planets only ($M_p > 0.1 \, M_J$). It is evident that several known exoplanet have $a/a_{Roche} < 2$ and subsequent short predicted remaining lifetimes. The distribution which peaks at $a/a_{Roche} \sim 3$ has been analysed before by Bonomo et al. (2017) amongst others. This could be an artefact caused by planets migrating inwards from highly eccentric orbits through tidal dissipation (Ford & Rasio 2006). Such planets would subsequently circularise which would lead to a bunch up at $3 a_{Roche}$. Disc driven migration on the other hand would result in an inner build up precisely at the Roche limit (Murray et al. 1998).

6.2. TOI-157b

TOI-157b is an inflated hot Jupiter with orbital period $P = 2.08$ days, mass $1.18 \pm 0.13 \, M_J$ and $R = 1.29 \pm 0.02 \, R_J$. The photometry from the ground-based follow-up and TESS is presented in Fig. B.2. The RVs are shown in Fig. 2, including two FEROS RVs which where not used in the analysis in the end, as they do not help constrain the amplitude of the RV curve when fitting an offset between CORALIE and FEROS.

The host star TOI-157 is a slightly evolved G-type subgiant with $T_{eff} = 5398 \pm 67$ K, $R_* = 1.17 \pm 0.02 \, R_\odot$ and $M_* = 0.95 \pm 0.02 \, M_\odot$. Through modelling the star with MIST we compute an age of $12.9^{+0.69}_{-1.4}$ Gyr. Given the evolved nature of TOI-157, the planet receives a considerable amount of insolation flux; 1032 times that of Earth, corresponding to an equilibrium temperature of 1588 ± 20K. TOI-157b has a separation of

just 0.03 AU to its sub-giant host star. Planets orbiting close-in ($a < 0.5$ AU) to evolved stars are very rare (Frink et al. 2001; Johnson et al. 2010; Jones et al. 2011) though TESS has provided several new detections around subgiants (TOI-120b, TOI-172b and TOI-197b: Nielsen et al. 2019; Brahm et al. 2019; Rodriguez et al. 2019; Huber et al. 2019; Wang et al. 2019).

6.3. TOI-169b

TOI-169b has the longest period of the three planets presented in this study with $P = 2.26$ days. It is a low-mass hot Jupiter with mass $0.79 \pm 0.06\ M_J$ and radius $R = 1.086^{+0.081}_{-0.048}\ R_J$. TOI-169 is found to be a main sequence G1-star with $T_{eff} = 5880 \pm 50$ K, $R_* = 1.288 \pm 0.020\ R_\odot$ and $M_* = 1.1477^{+0.069}_{-0.075}\ M_\odot$.

Despite having the longest orbital period of the three planets presented in this study, TOI-169b receives the highest insolation flux; 1403 times that of Earth, corresponding to an equilibrium temperature of 1715 ± 21 K. Figure 11 shows the known population of exoplanets plotted in insolation-radius space. TOI-169b is located right at the edge of the Neptune desert. Given its irradiation, TOI-169 is unusually dense, which could support a scenario of the atmospheric volatile layer being stripped away by photo-evaporation, to a point where the self-gravity of the planet is strong enough to withstand the atmospheric escape (Lopez & Fortney 2014; Mordasini et al. 2015). During this process, less massive planets could completely lose their outer layer and end up as a naked core at the bottom of the desert (Owen & Lai 2018), thus joining the large population of mainly *Kepler* planets seen in Fig. 11.

7. Conclusions

We have presented the discovery and mass determination of three new Jovian planets HIP 65Ab, TOI-157b, and TOI-169b from the TESS mission. We based our analysis on both 2-min cadence and FFI data from TESS spanning multiple Sectors in the first year of operations as well as numerous ground-based photometric observations. Light curves were modelled jointly with RVs from the CORALIE and FEROS spectrographs. Using SOAR speckle imaging we rule out close stellar companions for all three host stars.

HIP 65Ab is an ultra short period massive hot Jupiter with a period of 0.98 days, orbiting one component of a stellar binary. Despite the proximity to its host star, HIP 65Ab receives the least amount of radiation out of the three planets presented in this study. We find evidence that HIP 65Ab is spinning up its host star though tidal interaction. The planet's semi-major axis is less than twice the separation at which it would be destroyed by Roche lobe overflow. The predicted remaining lifetime ranges from 80 Myr to a few Gyr, assuming a reduced tidal dissipation quality factor of $Q'_s = 10^7 - 10^9$. TOI-157b and TOI-169b both receive more than 1000 times the Earth's insolation flux. TOI-157b orbits a sub-giant star with a 0.03 AU separation. TOI-169b is bordering the Neptune desert and can thus help solve the conundrum of which mechanisms are responsible for the shortage of close-in giant planets.

References

Alexander, R. D., & Armitage, P. J. 2009, ApJ, 704, 989
Anders, F., Khalatyan, A., Chiappini, C., et al. 2019, A&A, 628, A94
Armitage, P. J. 2007, ApJ, 665, 1381
Armstrong, D. J., de Mooij, E., Barstow, J., et al. 2016, Nat. Astron., 1, 0004
Artymowicz, P., & Lubow, S. H. 1994, ApJ, 421, 651
Bailey, E., & Batygin, K. 2018, ApJ, 866, L2
Bakos, G. Á., Torres, G., Pál, A., et al. 2010, ApJ, 710, 1724
Baraffe, I., Chabrier, G., & Barman, T. 2010, Rep. Prog. Phys., 73, 016901
Barnes, S. A. 2007, ApJ, 669, 1167
Batygin, K., & Stevenson, D. J. 2010, ApJ, 714, L238
Bayliss, D., Gillen, E., Eigmüller, P., et al. 2018, MNRAS, 475, 4467
Boisse, I., Moutou, C., Vidal-Madjar, A., et al. 2009, A&A, 495, 959
Bonomo, A. S., & Lanza, A. F. 2012, A&A, 547, A37
Bonomo, A. S., Desidera, S., Benatti, S., et al. 2017, A&A, 602, A107
Bourrier, V., Wheatley, P. J., Lecavelier des Etangs, A., et al. 2020, A&A, 635, A205
Brahm, R., Jordán, A., & Espinoza, N. 2017, PASP, 129, 034002
Brahm, R., Espinoza, N., Jordán, A., et al. 2019, AJ, 158, 45
Brown, D. J. A., Collier Cameron, A., Hall, C., Hebb, L., & Smalley, B. 2011, MNRAS, 415, 605
Brown, T. M., Baliber, N., Bianco, F. B., et al. 2013, PASP, 125, 1031
Cañas, C. I., Stefansson, G., Monson, A. J., et al. 2019, ApJ, 877, L29

Carmichael, T. W., Quinn, S. N., Mustill, A. J., et al. 2020, AJ, submitted [arXiv:2002.01943]

Carter, J. A., Rappaport, S., & Fabrycky, D. 2011, ApJ, 728, 139

Choi, J., Dotter, A., Conroy, C., et al. 2016, ApJ, 823, 102

Claret, A., & Bloemen, S. 2011, A&A, 529, A75

Collier Cameron, A., & Jardine, M. 2018, MNRAS, 476, 2542

Collins, K. A., Kielkopf, J. F., Stassun, K. G., & Hessman, F. V. 2017, AJ, 153, 77

Damiani, C., & Díaz, R. F. 2016, A&A, 589, A55

Demangeon, O. D. S., Faedi, F., Hébrard, G., et al. 2018, A&A, 610, A63

Díaz, M. R., Jenkins, J. S., Gandolfi, D., et al. 2020, MNRAS, 493, 973

Dotter, A. 2016, ApJS, 222, 8

Eastman, J., Gaudi, B. S., & Agol, E. 2013, PASP, 125, 83

Eastman, J. D., Rodriguez, J. E., Agol, E., et al. 2019, PASP, submitted [arXiv:1907.09480]

Eisner, N. L., Barragán, O., Aigrain, S., et al. 2020, MNRAS, 494, 750

Espinoza, N., Hartman, J. D., Bakos, G. Á., et al. 2019, AJ, 158, 63

Esposito, M., Armstrong, D. J., Gandolfi, D., et al. 2019, A&A, 623, A165

Faber, J. A., Rasio, F. A., & Willems, B. 2005, Icarus, 175, 248

Fabrycky, D., & Tremaine, S. 2007, ApJ, 669, 1298

Ford, E. B. 2006, ApJ, 642, 505

Ford, E. B., & Rasio, F. A. 2006, ApJ, 638, L45

Fressin, F., Torres, G., Charbonneau, D., et al. 2013, ApJ, 766, 81

Frink, S., Quirrenbach, A., Fischer, D., Röser, S., & Schilbach, E. 2001, PASP, 113, 173

Fukui, A., Narita, N., Tristram, P. J., et al. 2011, PASJ, 63, 287

Gaia Collaboration (Brown, A. G. A., et al.) 2018, A&A, 616, A1

Gelman, A., & Rubin, D. B. 1992, Stat. Sci., 7, 457

Gelman, A., Carlin, J. B., Stern, H. S., & Rubin, D. B. 2003, Bayesian Data Analysis, 2nd edn. (London: Chapman & Hall)

Gillon, M., Jehin, E., Fumel, A., Magain, P., & Queloz, D. 2013, Euro. Phys. J. Web of Conf., 47, 03001

Gillon, M., Anderson, D. R., Collier-Cameron, A., et al. 2014, A&A, 562, L3

Guerrero, N., Seager, S., Huang, C. X., et al. 2020, ApJS, submitted

Günther, M. N., Pozuelos, F. J., Dittmann, J. A., et al. 2019, Nat. Astron., 3, 1099

Hartman, J. D., Bakos, G. Á., Bayliss, D., et al. 2019, AJ, 157, 55

Hebb, L., Collier-Cameron, A., Triaud, A. H. M. J., et al. 2010, ApJ, 708, 224

Hellier, C., Anderson, D. R., Collier Cameron, A., et al. 2009, Nature, 460, 1098

Hellier, C., Anderson, D. R., Collier Cameron, A., et al. 2011, A&A, 535, L7

Henden, A., & Munari, U. 2014, Contrib. Astron. Observ. Skalnate Pleso, 43, 518

Høg, E., Fabricius, C., Makarov, V. V., et al. 2000, A&A, 355, L27

Huber, D., Chaplin, W. J., Chontos, A., et al. 2019, AJ, 157, 245

Jehin, E., Gillon, M., Queloz, D., et al. 2011, The Messenger, 145, 2

Jenkins, J. M., Chandrasekaran, H., McCauliff, S. D., et al. 2010, Proc. SPIE, 7740, 77400D

Jenkins, J. M., Twicken, J. D., McCauliff, S., et al. 2016, Proc. SPIE, 9913, 99133E

Jensen, E. 2013, Astrophysics Source Code Library [record ascl:1306.007]

Johnson, J. A., Aller, K. M., Howard, A. W., & Crepp, J. R. 2010, PASP, 122, 905

Jones, M. I., Jenkins, J. S., Rojo, P., & Melo, C. H. F. 2011, A&A, 536, A71

Jones, M. I., Brahm, R., Espinoza, N., et al. 2019, A&A, 625, A16

Jordán, A., Brahm, R., Espinoza, N., et al. 2019, AJ, 157, 100

Joss, P. C., & Rappaport, S. A. 1984, ARA&A, 22, 537

Kataria, T., Showman, A. P., Fortney, J. J., et al. 2015, ApJ, 801, 86

Kaufer, A., & Pasquini, L. 1998, Proc. SPIE, 3355, 844

Knapp, W. R. A., & Nanson, J. 2018, VizieR Online Data Catalog: 0/470

Kozai, Y. 1962, AJ, 67, 591

Kreidberg, L., Bean, J. L., Désert, J.-M., et al. 2014, ApJ, 793, L27

Lidov, M. L. 1962, Planet. Space Sci., 9, 719

Lindegren, L., Hernández, J., Bombrun, et al. 2018, A&A, 616, A2

Loeb, A., & Gaudi, B. S. 2003, ApJ, 588, L117

Lopez, E. D., & Fortney, J. J. 2014, ApJ, 792, 1

Lucy, L. B., & Sweeney, M. A. 1971, AJ, 76, 544

Lundkvist, M. S., Kjeldsen, H., Albrecht, S., et al. 2016, Nat. Commun., 7, 11201

Mandel, K., & Agol, E. 2002, ApJ, 580, L171

Mazeh, T., & Faigler, S. 2010, A&A, 521, L59

Mazeh, T., Holczer, T., & Faigler, S. 2016, A&A, 589, A75

McCormac, J., Pollacco, D., Skillen, I., et al. 2013, PASP, 125, 548

McCormac, J., Gillen, E., Jackman, J. A. G., et al. 2020, MNRAS, 493, 126

McCully, C., Volgenau, N. H., Harbeck, D.-R., et al. 2018, Proc. SPIE Conf. Ser., 10707, 107070K

Mordasini, C., Mollière, P., Dittkrist, K. M., Jin, S., & Alibert, Y. 2015, Int. J. Astrobiol., 14, 201

Morris, B. M., Hebb, L., Davenport, J. R. A., Rohn, G., & Hawley, S. L. 2017a, ApJ, 846, 99

Morris, B. M., Hawley, S. L., Hebb, L., et al. 2017b, ApJ, 848, 58

Murgas, F., Pallé, E., Zapatero Osorio, M. R., et al. 2014, A&A, 563, A41

Murray, N., Hansen, B., Holman, M., & Tremaine, S. 1998, Science, 279, 69

Murray-Clay, R. A., Chiang, E. I., & Murray, N. 2009, ApJ, 693, 23

Nagasawa, M., Ida, S., & Bessho, T. 2008, ApJ, 678, 498

Nagayama, T., Nagashima, C., Nakajima, Y., et al. 2003, SPIE Conf. Ser., 4841, 459

Narita, N., Nagayama, T., Suenaga, T., et al. 2013, PASJ, 65, 27

Nielsen, L. D., Bouchy, F., Turner, O., et al. 2019, A&A, 623, A100

Nielsen, L. D., Gandolfi, D., Armstrong, D. J., et al. 2020, MNRAS, 492, 5399

Niraula, P., Redfield, S., de Wit, J., et al. 2018, AJ, submitted [arXiv:1812.09227]

Oberst, T. E., Rodriguez, J. E., Colon, K. D., et al. 2017, AJ, 153, 97

Ogilvie, G. I., & Lin, D. N. C. 2007, ApJ, 661, 1180

Owen, J. E., & Lai, D. 2018, MNRAS, 479, 5012

Parmentier, V., Line, M. R., Bean, J. L., et al. 2018, A&A, 617, A110

Patience, J., Akeson, R. L., & Jensen, E. L. N. 2008, ApJ, 677, 616

Pearce, L. A., Kraus, A. L., Dupuy, T. J., et al. 2020, ApJ, 894, 115

Pecaut, M. J., & Mamajek, E. E. 2013, ApJS, 208, 9

Penev, K., Hartman, J. D., Bakos, G. Á., et al. 2016, AJ, 152, 127

Penev, K., Bouma, L. G., Winn, J. N., & Hartman, J. D. 2018, AJ, 155, 165

Queloz, D., Mayor, M., Udry, S., et al. 2001a, The Messenger, 105, 1

Queloz, D., Henry, G. W., Sivan, J. P., et al. 2001b, A&A, 379, 279

Ricker, G. R., Winn, J. N., Vanderspek, R., et al. 2015, J. Astron. Teles. Instrum. Sys., 1, 014003

Rodriguez, J. E., Quinn, S. N., Huang, C. X., et al. 2019, AJ, 157, 191

Santerne, A., Moutou, C., Tsantaki, M., et al. 2016, A&A, 587, A64

Santos, N. C., Mayor, M., Naef, D., et al. 2002, A&A, 392, 215

Schlafly, E. F., & Finkbeiner, D. P. 2011, ApJ, 737, 103

Schlegel, D. J., Finkbeiner, D. P., & Davis, M. 1998, ApJ, 500, 525

Schuessler, M., Caligari, P., Ferriz-Mas, A., Solanki, S. K., & Stix, M. 1996, A&A, 314, 503

Shporer, A. 2017, PASP, 129, 072001

Shporer, A., Wong, I., Huang, C. X., et al. 2019, AJ, 157, 178

Sing, D. K., Pont, F., Aigrain, S., et al. 2011, MNRAS, 416, 1443

Skrutskie, M. F., Cutri, R. M., Stiening, R., et al. 2006, AJ, 131, 1163

Smith, J. C., Stumpe, M. C., Van Cleve, J. E., et al. 2012, PASP, 124, 1000

Snellen, I. A. G., de Mooij, E. J. W., & Albrecht, S. 2009, Nature, 459, 543

Stassun, K. G., Oelkers, R. J., Pepper, J., et al. 2018, AJ, 156, 102

Stassun, K. G., Oelkers, R. J., Paegert, M., et al. 2019, AJ, 158, 138

Stumpe, M. C., Smith, J. C., Van Cleve, J. E., et al. 2012, PASP, 124, 985

Stumpe, M. C., Smith, J. C., Catanzarite, J. H., et al. 2014, PASP, 126, 100

Suárez Mascareño, A., Rebolo, R., González Hernández, J. I., & Esposito, M. 2015, MNRAS, 452, 2745

Suárez Mascareño, A., Rebolo, R., González Hernández, J. I., & Esposito, M. 2017, MNRAS, 468, 4772

Šubjak, J., Sharma, R., Carmichael, T. W., et al. 2020, AJ, 159, 151

Szabó, G. M., & Kiss, L. L. 2011, ApJ, 727, L44

Tokovinin, A. 2018, PASP, 130, 035002

van Kerkwijk, M. H., Rappaport, S. A., Breton, R. P., et al. 2010, ApJ, 715, 51

Vines, J. I., Jenkins, J. S., Acton, J. S., et al. 2019, MNRAS, 489, 4125

Wang, S., Jones, M., Shporer, A., et al. 2019, AJ, 157, 51

Wheatley, P. J., West, R. G., Goad, M. R., et al. 2018, MNRAS, 475, 4476

Wolter, U., Schmitt, J. H. M. M., Huber, K. F., et al. 2009, A&A, 504, 561

Wong, I., Shporer, A., Daylan, T., et al. 2020, AJ, submitted [arXiv:2003.06407]

Wright, E. L., Eisenhardt, P. R. M., Mainzer, A. K., et al. 2010, AJ, 140, 1868

Wu, Y., & Murray, N. 2003, ApJ, 589, 605

Yee, S. W., Petigura, E. A., & von Braun, K. 2017, ApJ, 836, 77

Yee, S. W., Winn, J. N., Knutson, H. A., et al. 2020, ApJ, 888, L5

Zhou, G., Huang, C. X., Bakos, G. Á., et al. 2019, AJ, 158, 141

Ziegler, C., Tokovinin, A., Briceño, C., et al. 2020, AJ, 159, 19

[1] Geneva Observatory, University of Geneva, Chemin des Mailettes 51, 1290 Versoix, Switzerland
e-mail: louise.nielsen@unige.ch

[2] Facultad de Ingeniería y Ciencias, Universidad Adolfo Ibáñez, Av. Diagonal las Torres 2640, Peñalolén, Santiago, Chile

[3] Millennium Institute for Astrophysics, Chile

[4] Space Telescope Science Institute, 3700 San Martin Drive, Baltimore, MD 21218, USA

[5] Department of Physics and Kavli Institute for Astrophysics and Space Research, MIT, Cambridge, MA 02139, USA

[6] NSF Graduate Research Fellow, Steward Observatory, University of Arizona, Tucson, AZ 85721, USA

[7] Center for Astrophysics | Harvard & Smithsonian, 60 Garden Street, Cambridge, MA 02138, USA

[8] Department of Earth, Atmospheric and Planetary Sciences, MIT, Cambridge, MA 02139, USA

[9] Department of Aeronautics and Astronautics, MIT, Cambridge, MA 02139, USA

[10] Department of Astrophysical Sciences, Princeton University, 4 Ivy Lane, Princeton, NJ 08544, USA

[11] NASA Ames Research Center, Moffett Field, CA 94035, USA

[12] Department of Physics and Astronomy, University of Leicester, University Road, Leicester, LE1 7RH, UK

[13] NASA Goddard Space Flight Center, 8800 Greenbelt Rd, Greenbelt, MD 20771, USA

[14] University of Maryland, Baltimore County, 1000 Hilltop Cir, Baltimore, MD 21250, USA

[15] Astrobiology Research Unit, Université de Liège, 19C Allée du 6 Août, 4000 Liège, Belgium

[16] Oukaimeden Observatory, High Energy Physics and Astrophysics Laboratory, Cadi Ayyad University, Marrakech, Morocco

[17] Cerro Tololo Inter-American Observatory, Casilla 603, La Serena, Chile

[18] Dept. of Physics, University of Warwick, Gibbet Hill Road, Coventry CV4 7AL, UK

[19] Centre for Exoplanets and Habitability, University of Warwick, Gibbet Hill Road, Coventry CV4 7AL, UK

[20] Caltech IPAC – NASA Exoplanet Science Institute 1200 E. California Ave, Pasadena, CA 91125, USA

[21] George Mason University, 4400 University Drive, Fairfax, VA 22030, USA

[22] Institute of Planetary Research, German Aerospace Center, Rutherfordstrasse 2, 12489 Berlin, Germany

[23] Physics Department and Tsinghua Centre for Astrophysics, Tsinghua University, Beijing 100084, PR China

[24] Centre for Astrophysics, University of Southern Queensland, Toowoomba 4350, Australia

[25] Max-Planck-Institut für Astronomie, Königstuhl 17, Heidelberg 69117, Germany

[26] Space Sciences, Technologies and Astrophysics Research (STAR) Institute, Université de Liège, 19C Allée du 6 Août, 4000 Liège, Belgium

[27] Departamento de Astronomía, Universidad de Chile, Camino El Observatorio 1515, Las Condes, Santiago, Chile

[28] Centro de Astrofísica y Tecnologías Afines (CATA), Casilla 36-D, Santiago, Chile

[29] Department of Physics and Astronomy, University of Louisville, Louisville, KY 40292, USA

[30] Department of Physics and Astronomy, University of North Carolina at Chapel Hill, Chapel Hill, NC 27599-3255, USA

[31] Space Research Institute, Austrian Academy of Sciences, Schmiedlstr. 6, 8042 Graz, Austria

[32] The University of Tokyo, 7-3-1 Hongo, Bunkyō, Tokyo 113-8654, Japan

[33] Instituto de Astronomía, Universidad Católica del Norte, Angamos 0610, Antofagasta 1270709, Chile

[34] Astrobiology Center, 2-21-1 Osawa, Mitaka, Tokyo 181-8588, Japan

[35] JST, PRESTO, 2-21-1 Osawa, Mitaka, Tokyo 181-8588, Japan

[36] National Astronomical Observatory of Japan, 2-21-1 Osawa, Mitaka, Tokyo 181-8588, Japan

[37] Instituto de Astrofísica de Canarias (IAC), 38205 La Laguna, Tenerife, Spain

[38] Komaba Institute for Science, The University of Tokyo, 3-8-1 Komaba, Meguro, Tokyo 153-8902, Japan

[39] Las Campanas Observatory, Carnegie Institution of Washington, Colina el Pino, Casilla 601 La Serena, Chile

[40] Institute for Computational Science, University of Zurich, Winterthurerstr. 190, 8057 Zurich, Switzerland

[41] Hazelwood Observatory, Australia

[42] Perth Exoplanet Survey Telescope, Perth, Western Australia, Australia

[43] NASA Sagan Fellow, Department of Astronomy, Unversity of Texas at Austin, Austin, TX, USA

[44] Mt. Stuart Observatory, New Zealand

[45] Dunlap Institute for Astronomy and Astrophysics, University of Toronto, 50 St. George Street, Toronto, Ontario M5S 3H4, Canada

Appendix A: RV data

Table A.1. Radial velocity measurements from CORALIE and FEROS for HIP 65A.

BJD (−2 400 000)	RV (m s^{-1})	σ_{RV} (m s^{-1})	BIS (m s^{-1})	Instrument
58 382.793749	22 105.0	25.5	−40.7	CORALIE
58 406.764434	20 526.8	66.6	−118.2	CORALIE
58 408.788981	20 652.1	28.6	−134.2	CORALIE
58 410.498946	21 177.3	31.6	−64.6	CORALIE
58 410.586650	20 825.2	31.5	−49.1	CORALIE
58 410.732244	20 533.6	31.2	21.7	CORALIE
58 411.498626	21 082.4	41.5	−51.7	CORALIE
58 411.591838	20 749.7	32.7	−169.6	CORALIE
58 411.648374	20 664.0	28.6	−73.4	CORALIE
58 417.594656	20 602.4	43.3	−274.9	CORALIE
58 419.531857	20 635.3	31.1	−71.7	CORALIE
58 426.579955	20 998.7	34.5	−88.5	CORALIE
58 465.662441	20 607.2	20.7	−63.9	CORALIE
58 478.592577	21 109.9	14.5	−42.7	CORALIE
58 479.593054	21 206.5	15.5	−47.2	CORALIE
58 487.570334	21 766.1	18.0	−71.7	CORALIE
58 500.538320	22 047.5	28.3	−32.1	CORALIE
58 408.66413	20 733.1	10.8	−35	FEROS
58 411.74045	20 675.5	9.3	−29	FEROS
58 412.64109	20 671.7	8.3	−52	FEROS
58 413.54882	20 791.6	7.8	−29	FEROS
58 414.63269	20 630.9	8.3	−35	FEROS
58 415.63086	20 635.0	9.7	−4	FEROS
58 416.59652	20 608.9	8.3	15	FEROS
58 418.59589	20 662.7	8.3	−40	FEROS
58 419.56945	20 659.0	8.6	−14	FEROS
58 423.65772	21 140.9	8.7	−57	FEROS
58 424.57114	20 896.8	8.4	−26	FEROS
58 428.72879	21 898.1	9.5	−15	FEROS
58 430.68560	21 856.6	8.8	15	FEROS
58 450.63188	21 655.5	8.6	−17	FEROS
58 451.56707	21 856.7	9.3	55	FEROS
58 451.58556	21 762.3	8.1	−35	FEROS
58 452.57292	21 747.4	8.8	−9	FEROS

**Table A.2.** Radial velocity measurements from CORALIE and FEROS for TOI-157.

BJD (−2 400 000)	RV (m s^{-1})	σ_{RV} (m s^{-1})	BIS (m s^{-1})	Instrument
58 394.715066	−8782.2	118.7	−130.7	CORALIE
58 397.866695	−8941.8	72.6	−59.6	CORALIE
58 414.670583	−8868.6	52.6	15.3	CORALIE
58 417.691914	−8498.7	62.6	−35.8	CORALIE
58 418.770424	−8855.5	55.2	−14.9	CORALIE
58 419.814201	−8543.7	53.7	−36.5	CORALIE
58 427.857757	−8658.9	53.5	−7.8	CORALIE
58 433.659427	−8876.8	75.0	−105.2	CORALIE
58 455.780420	−8742.2	44.4	−120.3	CORALIE
58 456.769193	−8860.9	90.3	−117.4	CORALIE
58 457.708950	−8681.1	73.9	38.3	CORALIE
58 458.705351	−8951.0	79.1	−124.8	CORALIE
58 460.665537 [a]	−9183.8	211.2	414.9	CORALIE
58 461.712853	−8534.8	57.9	−40.7	CORALIE
58 462.651604	−8907.4	58.5	−3.4	CORALIE
58 463.574905	−8503.6	59.6	−12.2	CORALIE
58 463.809868	−8526.8	50.3	−130.3	CORALIE
58 464.562176	−8926.0	51.5	106.0	CORALIE
58 464.749963	−8958.1	65.2	64.1	CORALIE
58 467.599544	−8571.1	61.5	−15.2	CORALIE
58 471.590055	−8625.6	57.7	−90.1	CORALIE
58 474.675323	−8691.5	50.8	44.9	CORALIE
58 475.657076	−8538.2	43.6	139.4	CORALIE
58 486.705154	−8543.7	54.0	−47.5	CORALIE
58 381.883623	−8663.9	16.3	25	FEROS
58 383.881139	−8672.1	14.9	61	FEROS

Notes. The two FEROS RVs were not included in the global modelling of the system. [a]Low S/N RV-measurement from BJD 58 460.665537, not included in global analysis.

Table A.3. Radial velocity measurements from CORALIE and FEROS for TOI-169.

| BJD (−2 400 000)	RV (m s^{-1})	σ_{RV} (m s^{-1})	BIS (m s^{-1})	Instrument
58 411.74975	43 526.9	14.0	68	FEROS
58 414.79857	43 754.4	16.3	−66	FEROS
58 418.63748	43 562.4	12.1	17	FEROS
58 419.65549	43 671.5	10.6	−28	FEROS
58 423.68635	43 716.1	11.5	23	FEROS
58 428.71918	43 688.5	12.7	15	FEROS
58 429.67408	43 529.5	11.2	5	FEROS
58 430.75367	43 716.2	11.5	−7	FEROS
58 450.72036	43 696.4	10.4	56	FEROS
58 451.57625	43 586.1	9.8	29	FEROS
58 648.913708	43 623.24	63.7	119.9	CORALIE
58 657.885639	43 570.95	38.2	−27.9	CORALIE
58 666.832642	43 601.87	55.4	−66.4	CORALIE
58 669.821282	43 720.12	41.9	97.4	CORALIE
58 677.860677	43 523.81	53.0	−17.5	CORALIE
58 679.934507	43 490.82	42.3	18.9	CORALIE

Appendix B: Light curves
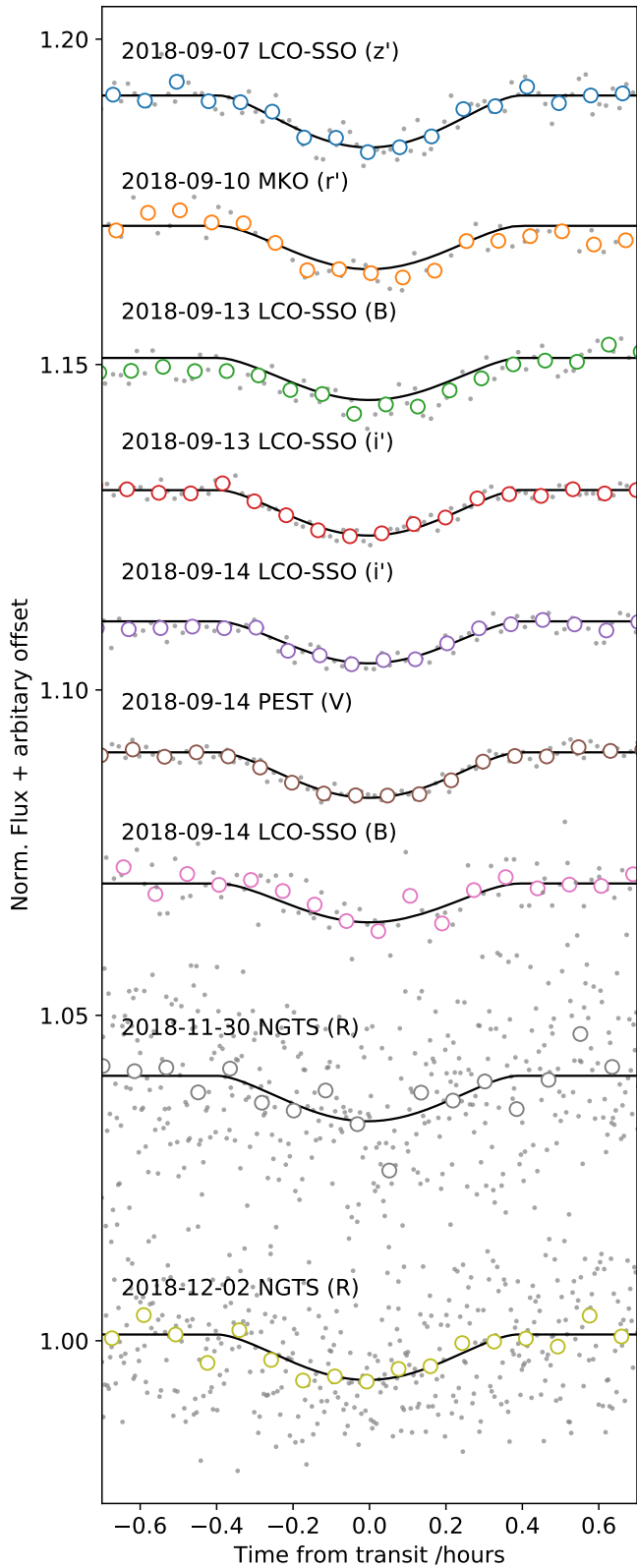
Fig. B.1. Ground based photometric follow-up data for HIP 65Ab from LCO-SSO, MKO, PEST and NGTS. The open circles are data binned to 5 min.
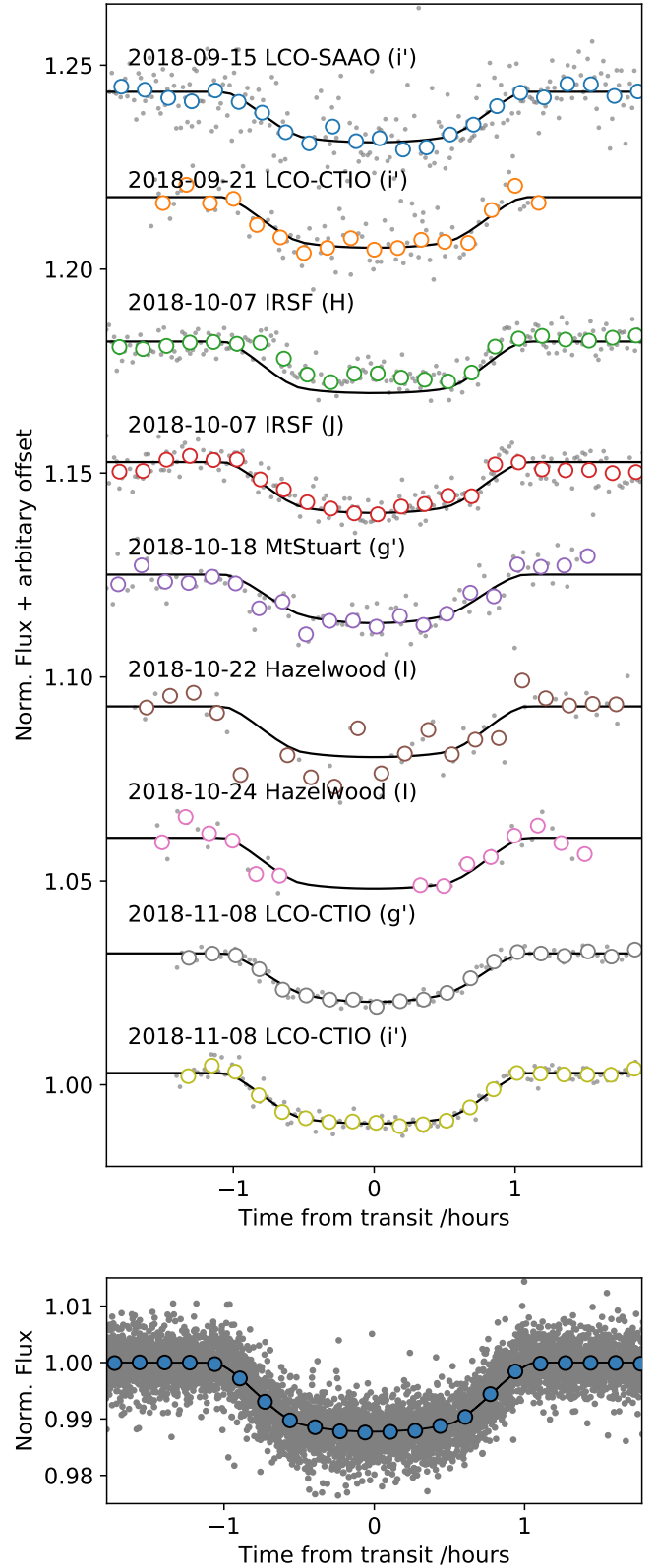
Fig. B.2. *Top*: ground based photometric follow-up data for TOI-157b. The open circles are data binned to 10 min. *Bottom*: phase folded transit light curve for TOI-157b including TESS data and follow-up photometry in grey. The blue circles are the same data binned to 10 min.
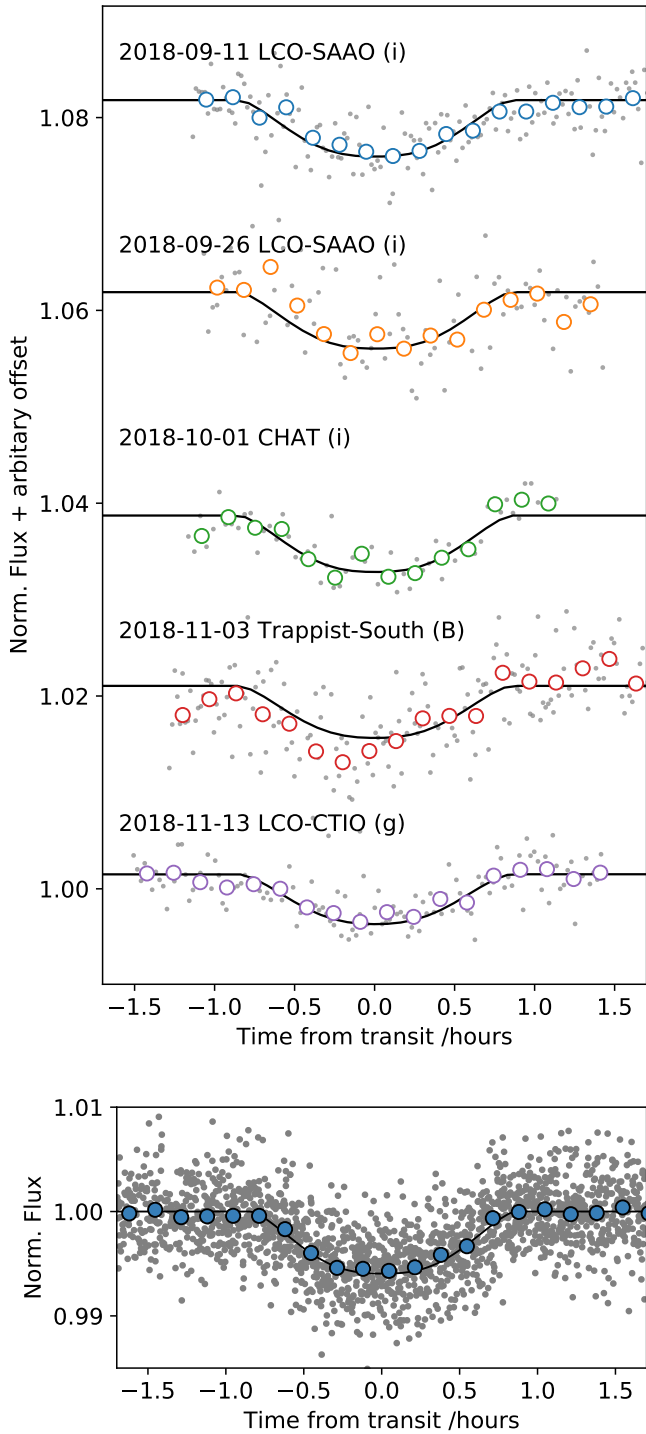
Fig. B.3. *Top*: ground based photometric follow-up data for TOI-169 The open circles are data binned to 10 min. *Bottom*: phase folded transit light curve for TOI-169 including TESS data and follow-up photometry, also with 10 min bins over-plotted as blue circles.